

Viscous heat backflow and temperature resonances in extreme thermal conductors

Jan Dragašević^{1,*} and Michele Simoncelli^{1,†}

¹*Theory of Condensed Matter Group, Cavendish Laboratory, University of Cambridge (UK)*

We demonstrate that non-diffusive, fluid-like heat transport, such as heat backflowing from cooler to warmer regions, can be induced, controlled, and amplified in extreme thermal conductors such as graphite and hexagonal boron nitride. We employ the viscous heat equations, *i.e.* the thermal counterpart of the Navier-Stokes equations in the laminar regime, to show with first-principles quantitative accuracy that a finite thermal viscosity yields steady-state heat vortices, and governs the magnitude of transient temperature waves. Finally, we devise strategies that exploit devices' boundaries and resonance to amplify and control heat hydrodynamics, paving the way for novel experiments and applications in next-generation electronic and phononic technologies.

Introduction.—Crystals with ultrahigh thermal conductivity, such as graphite[1–4] and monoisotopic layered hexagonal boron nitride (h¹¹BN) [5, 6], are critical for copious thermal-management applications in e.g. electronics and phononics [7, 8]. These materials are also of fundamental scientific interest, since they can host heat-transport phenomena that violate Fourier's diffusive law [9–12]. For example, striking hydrodynamic-like phenomena such as temperature waves—where heat transiently backflows from cooler to warmer regions—have recently been observed in graphite up to ~ 200 K [13][14]. While these phenomena hold great potential for heat-management technologies [7, 9], they are weak and challenging to observe. Thus, technologically exploiting heat hydrodynamics requires unraveling the fundamental physics determining its emergence and how to control it.

Hitherto, the theoretical analysis of heat hydrodynamics has been done relying on the linearized Peierls-Boltzmann transport equation (LBTE) [15] and on first-principles simulations [7, 9, 16–20]. These works have provided microscopic insights on hydrodynamic heat transport in three-dimensional [3, 5, 13, 21–24] and two-dimensional [3, 19, 20, 25–30] materials, quantitatively discussing how this emerges from the predominance of momentum-conserving (normal) phonons' collisions over momentum-relaxing (Umklapp) collisions. Under these conditions, the phonon's local equilibrium is described by the drifting distribution, $N_{\mathbf{q},s}^D[T(\mathbf{r},t), \mathbf{u}(\mathbf{r},t)] = [\exp(\frac{\hbar}{k_B T(\mathbf{r},t)}[\omega_{\mathbf{q}s} - \mathbf{q} \cdot \mathbf{u}(\mathbf{r},t)]) - 1]^{-1}$ ($\hbar\omega_{\mathbf{q}s}$ is the energy of the phonon with crystal momentum $\hbar\mathbf{q}$ and mode s), which is parametrized not only by a local temperature $T(\mathbf{r},t)$ (emerging from the conservation of energy in all phonon collisions), but also by a drift velocity $\mathbf{u}(\mathbf{r},t)$ that emerges from the conservation of crystal momentum in the dominant normal collisions. While the LBTE has provided insights on heat hydrodynamic phenomena such as second sound (temperature oscillations) [11, 13, 25] and Poiseuille-like heat flow [10, 19, 23, 31–33], its complexity and high computational cost (stemming from microscopically

resolving how every phonon mode $\mathbf{q}s$ interacts and contribute to transport) hinders its use to explore new hallmarks of heat hydrodynamics. Recent research has been focused on developing mesoscopic models that capture the physics governing heat hydrodynamics at reduced complexity and cost; in practice, these are obtained marginalizing the microscopic (phonon) degrees of freedom in the LBTE, thus describe only the evolution of local-equilibrium fields (T and \mathbf{u}) [34–38].

Viscous heat equations.—Ref. [37] has shown how the symmetries of the microscopic LBTE imply that two transport coefficients are needed to describe thermal transport comprehensively from the diffusive to the hydrodynamic regime. The first one is the well known thermal conductivity tensor κ^{ij} (i, j are Cartesian indexes), which originates from the odd-parity part of the LBTE's solution, and quantifies the response of the crystal to a temperature perturbation. The second one, the thermal viscosity tensor μ^{ijkl} , emerges from the even-parity part; this is usually neglected but becomes relevant in the hydrodynamic regime, quantifying the response to a drift-velocity perturbation. Conductivity and viscosity parametrize two coupled viscous heat equations (VHE) for $T(\mathbf{r},t)$ and $\mathbf{u}(\mathbf{r},t)$ (repeated indexes are summed):

$$C \frac{\partial T(\mathbf{r},t)}{\partial t} + \alpha^{ij} \frac{\partial u^j(\mathbf{r},t)}{\partial r^i} - \kappa^{ij} \frac{\partial^2 T(\mathbf{r},t)}{\partial r^i \partial r^j} = \dot{q}(\mathbf{r},t), \quad (1)$$

$$A^{ij} \frac{\partial u^j(\mathbf{r},t)}{\partial t} + \beta^{ij} \frac{\partial T(\mathbf{r},t)}{\partial r^j} - \mu^{ijkl} \frac{\partial^2 u^k(\mathbf{r},t)}{\partial r^j \partial r^l} = -\gamma^{ij} u^j(\mathbf{r},t), \quad (2)$$

where C is the specific heat; $A^{ij} = A^i \delta^{ij}$ is a matrix having zero off-diagonal elements and the specific momentum in direction i , A^i , on the diagonal; α^{ij} and β^{ij} are coupling tensors that originate from the relation between energy and crystal momentum for phonons; $\dot{q}(\mathbf{r},t)$ describes the energy exchange with a localized external heater; the dissipative term $-\gamma^{ij} u^j(\mathbf{r},t)$ accounts for the presence of Umklapp processes (this term is weak in the hydrodynamic regime and becomes strong in the diffusive regime, implying that in the latter the VHE reduce to Fourier's law [37]). All these parameters can be determined exactly from the LBTE accounting for the actual phonon band structure and full collision matrix with first-principles accuracy, see Supplementary Material (SM). Finally, we recall that within the VHE the total heat flux (\mathbf{Q}^{TOT}) is de-

*Current address: Physics Department, University of Zagreb (HR)

† ms2855@cam.ac.uk

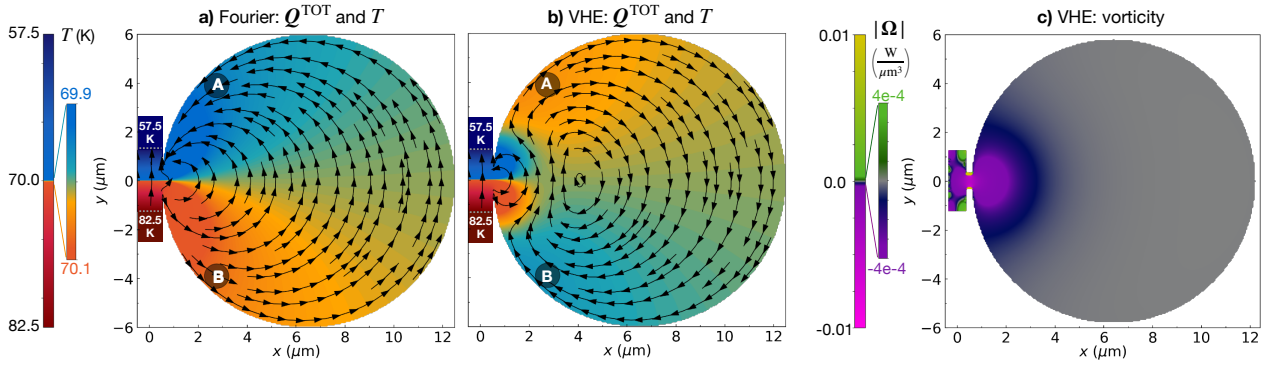


FIG. 1. **Steady-state viscous heat backflow.** In-plane (x - y) heat flow (streamlines) and temperature (colormap) in a tunnel-chamber device made of graphite. Panel **a** (**b**) shows the solution of Fourier's equation (VHE) in the presence of a temperature gradient applied to the tunnel ($T = 70 \pm 12.5$ K at $y = \mp 1.25 \mu m$), the other boundaries are adiabatic, *i.e.* $\nabla T \cdot \hat{n} = 0$, where \hat{n} is the versor orthogonal to the boundary and, in the VHE, "slipping" ($\mathbf{u} \cdot \hat{n} = 0$). In Fourier's case (**a**), the direction of the temperature gradient in the chamber mirrors that in the tunnel ($T_A < T_B$). In contrast, the VHE (**b**) allows for the emergence of viscous backflow, whose hallmark is a temperature gradient in the chamber reversed compared to the tunnel ($T_A > T_B$). Panel **c**), vorticity of the VHE heat flux, $\nabla \times \mathbf{Q}^{TOT}$; the vorticity for Fourier's flux (not reported) is trivially zero.

terminated by temperature gradient and drift velocity, *i.e.*, $\mathbf{Q}^{TOT} = \mathbf{Q}^\delta + \mathbf{Q}^D$ where $Q^{\delta,i} = -\kappa^{ij} \nabla^j T$ and $Q^{D,i} = \alpha^{ij} u^j$.

The VHE encompass Fourier's law and temperature waves [39, 40] as special limiting cases. Fourier's limit emerges when Umklapp dissipation is strong and viscous effects are negligible [37][41]. Temperature waves, instead, are obtained in the transient inviscid limit ($\mu^{ijkl} = 0 \forall i, j, k, l$), where the VHE reduce to the established dual-phase-lag equation (DPLE) [39, 40], see SM I for a proof (we also note that the DPLE encompasses Cattaneo's second-sound [42] equation as a special case). Both the Fourier and DPLE limits are obtained when viscous effects are negligible, the former in the steady-state and the latter in the transient domain. Thus, understanding how thermal viscosity affects temperature waves (transient heat backflow), and the possible emergence of viscous heat backflow in the steady state, are open fundamental questions. Here we address these questions, investigating from first principles how to induce, amplify, and control viscous heat hydrodynamics in graphite at various isotopic purities, as well as in $h^{11}BN$ [43].

Steady-state viscous heat backflow.—In Fig. 1 we investigate how viscosity affects steady-state thermal transport by comparing the numerical solution of Fourier's (inviscid) equation (panel **a**) with that of the viscous VHE (panel **b**). We consider a graphitic device having tunnel-chamber geometry[44], which promotes vortical hydrodynamic behavior (more on this later). We highlight that the VHE temperature profile in the chamber is reversed compared to the profile in the tunnel, a behavior completely opposite to that predicted by Fourier's law. Panel **c** shows that this temperature inversion—which in principle can be detected in thermal-imaging experiments [45–49]—occurs in the presence of viscous vortical flow, when heat backflows against the temperature gradient. In SM II we show that heat vortices are not limited to graphite, predicting them also in $h^{11}BN$ around 60 K.

To see how the emergence of the heat backflow vortex

in Fig. 1 requires the presence of a finite thermal viscosity, we start from Eqs. (1,2) in the steady-state and focus on geometries for which transport is isotropic (e.g. graphite and $h^{11}BN$ in the in-plane directions). Hereafter Cartesian indexes will be omitted for tensors that are proportional to the identity in the in-plane directions, see SM IX. Then, considering the inviscid limit, Eq. (2) reduces to $\beta \nabla T(\mathbf{r}, t) = -\gamma \mathbf{u}(\mathbf{r}, t)$, and using this in Eq. (1) readily shows that this inviscid limit is governed by a Fourier-like irrotational equation, where the total heat flux is exclusively determined by the temperature gradient and thus vortices and backflow cannot emerge [50]. In contrast, when a non-zero thermal viscosity is considered in Eq. (2), the drift velocity is no longer proportional to the temperature gradient, and thus the total heat flux $\mathbf{Q}^{TOT} = \mathbf{Q}^\delta + \mathbf{Q}^D = -\kappa \nabla T + \alpha \mathbf{u}$ cannot be simplified to an irrotational expression. This demonstrates that having a non-zero viscosity is necessary to have non-zero vorticity and observe steady-state viscous heat backflow. However, having non-zero viscosity is not sufficient to observe heat backflow; in fact, one also needs a device's geometry and boundary conditions that ensure the presence of non-zero second derivative of the drift velocity, *i.e.*, of a total heat flux with non-zero vorticity. In this regard, we discuss in SM III how the tunnel-chamber geometry and 'slipping' boundaries (corresponding to reflective phonon-boundary scattering [18, 51, 52], [53]) can drive non-homogeneities in the drift velocity that are sufficient to have viscous heat backflow and temperature inversion. In SM IV we discuss how such backflow depends on device's size, average temperature, and isotopic disorder.

Transient viscous heat backflow.—Recent experiments in graphite have observed heat backflowing against the temperature gradient only in the time-dependent domain, in the form of second sound [11, 13] or lattice cooling [12]. The pioneering theoretical analyses have been performed relying on the microscopic LBTE [11–13, 54, 55] without resolving effects induced by the ther-

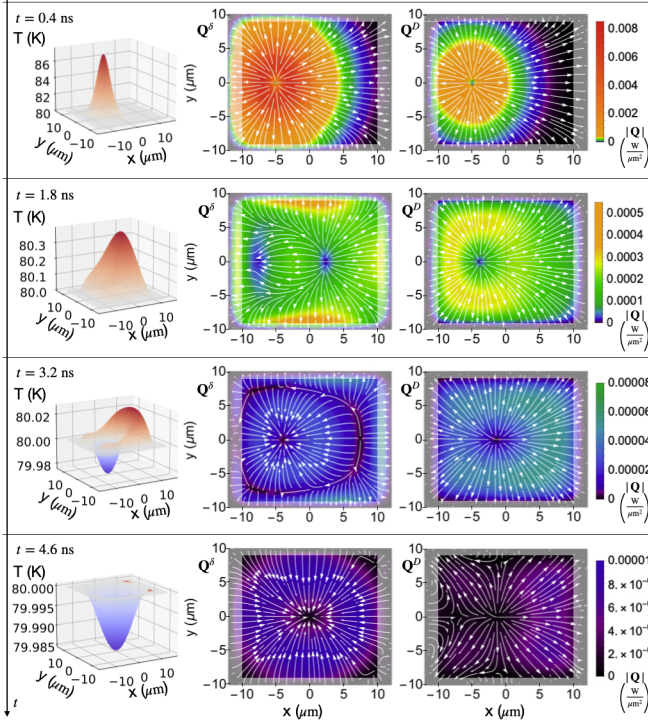


FIG. 2. **Transient viscous heat backflow.** Columns show temperature (left), temperature-gradient heat flux (Q^δ , center), and drifting heat flux (Q^D , right) at different times (relaxation starts at $t=0.4$ ns, see text), and are obtained solving the VHE in a graphitic device thermalised at 80 K in the shaded boundary regions. In the 2D plots, color is the heat-flux modulus, and white streamlines show it direction.

mal viscosity, or relying on the inviscid mesoscopic DPLe [39, 40, 56–61]. It is therefore natural to wonder how the viscous heat backflow emerging from the VHE behaves in the time domain, and more precisely if there is a relationship between temperature waves and transient viscous heat backflow. Therefore, we perform the time-dependent simulation shown in Fig. 2. We consider a rectangular device that is initially at equilibrium ($T=80$ K [62] and $\mathbf{u}=0$ everywhere); we perturb it with a heater localized at $(x_c = 5\mu\text{m}, 0)$ for $0 < t < t_{\text{heat}} = 0.4$ ns ($\dot{q}(\mathbf{r}, t) = \mathcal{H} \cdot \theta(t_{\text{heat}} - t) \exp\left[-\frac{(x+x_c)^2}{2\sigma_x^2} - \frac{y^2}{2\sigma_y^2}\right]$, see Eq. (1) and note [63]); at $t=t_{\text{heat}}$ we switch off the heater and monitor the relaxation to equilibrium. The device is always thermalised at the boundaries ($T=80\text{K}$ and $\mathbf{u}=0$), see Ref. [48] for an experimental example of this boundary condition, and SM VI for details on how boundary conditions (average temperature and thermalisation lengthscale), size, and isotopic disorder affect the relaxation. The VHE evolution of the temperature field (first column in Fig. 2) shows an oscillatory behavior, with the local appearance of temperature values lower than the initial temperature. In contrast, we show in SM VII that in Fourier’s law a positive temperature perturbation relaxes remaining non-negative with respect to the initial equilibrium value (a consequence of the smoothing property of the diffusion equation [64]).

To understand what drives the emergence of heat backflow, we analyze the evolution of the heat-flux components Q^δ and Q^D . Their streamlines in the second and third column of Fig. 2 show that Q^δ and Q^D can assume opposite directions during the relaxation, with the drifting flux $Q^D \propto \mathbf{u}$ backflowing against the temperature-gradient flux $Q^\delta \propto -\nabla T$. This is a consequence of the delayed coupling between Q^δ and Q^D in the VHE (1,2), which in the inviscid limit ($\mu=0$) reduces exactly to the lagged relationship between heat flux and temperature gradient described by the dual-phase-lag model [40]. Specifically, we show in SM I that in the inviscid limit $Q^{TOT}(\mathbf{r}, t + \tau_Q) = -\kappa \nabla T(\mathbf{r}, t + \tau_T)$, where $\tau_Q = A/\gamma$ is the delay between the application of a temperature gradient and the appearance of a heat flux, and $\tau_T = \kappa A/(\alpha\beta + \kappa\gamma)$ is the time needed to create temperature gradient from an established heat flux. This also shows that while steady-state heat backflow can emerge exclusively as a consequence of a finite viscosity, time-dependent heat backflow does not necessarily require viscosity to appear (SM VII). Nevertheless, we will show that it is necessary to consider viscous effects to quantitatively explain experiments.

Resonant amplification of temperature waves.—The temperature waves observed in Fig. 2 have a small amplitude and consequently are difficult to be detected. Nevertheless, they are expected to exhibit resonant amplification when driven with a perturbation periodic in time, and this could be exploited to facilitate their observation and control. Therefore, we investigate the behavior of the device in Fig. 2 when driven with a periodic perturbation. Considering the analogies between temperature and mechanical waves, we applied to the device in Fig. 2 a perturbation mathematically similar to the (1,2) mode of a loaded rectangular membrane,

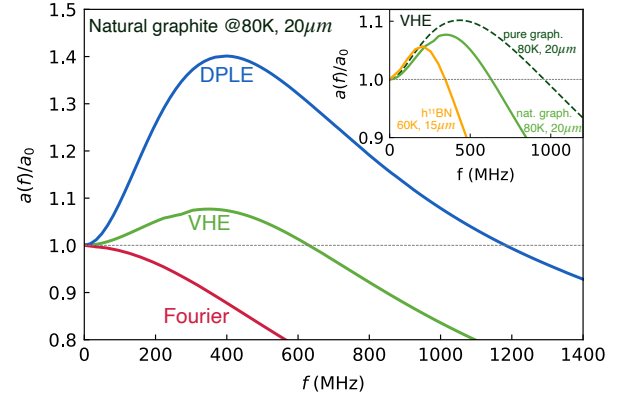


FIG. 3. **Resonant amplification of temperature waves** in graphite at natural isotopic disorder (98.9% ^{12}C , 1.1% ^{13}C) and around $T=80\text{K}$. The prediction from the viscous VHE is green, blue is the inviscid DPLe, and red is Fourier’s law. Inset, the VHE predict that isotopically purified graphite (99.9% ^{12}C , 0.1% ^{13}C , dashed dark green) features a stronger resonant amplification compared to natural graphite (solid green); in addition, analogous signatures are predicted to appear in h^{11}BN , around $T=60\text{K}$ in $15\mu\text{m}$ -long devices.

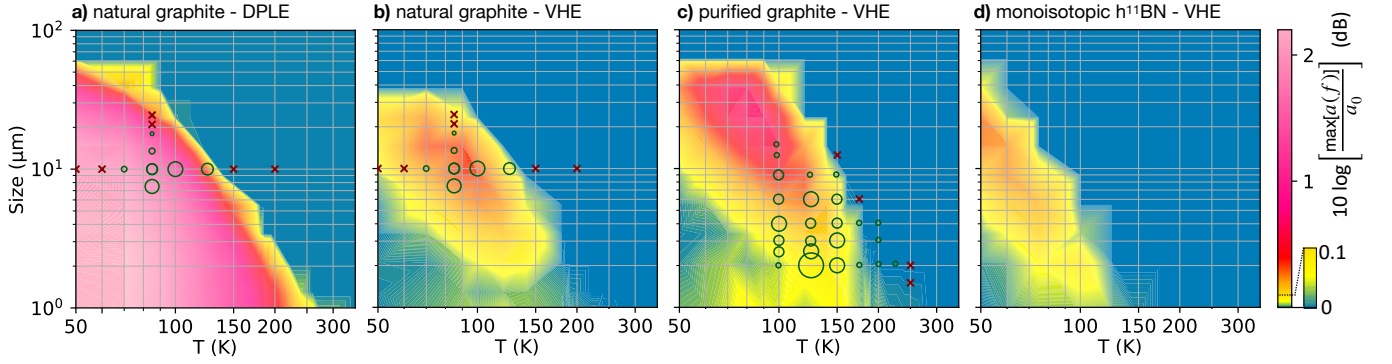


FIG. 4. **Maximum resonant amplification as a function of size, temperature, and isotopic disorder.** The colormaps show the maximum resonant amplification (see text) as a function of the characteristic size of the rectangular device [65] and of the temperature around which the perturbation is applied. Panels **a,b** refer to natural graphite, **a**) is the DPLE and **b**) the VHE. Empty green circles have an area proportional to the hydrodynamic strength [66] measured in experiments by Huberman *et al.* [11] for natural samples, and by Ding *et al.* [13] for isotopically purified samples; the red crosses correspond to diffusive behavior (no hydrodynamics). The VHE (**b**) capture the temperatures and lengthscales at which hydrodynamic behavior appears; in contrast, the inviscid DPLE departs from experiments at low temperature. Panel **c**), VHE hydrodynamic behavior in isotopically purified graphite, in broad agreement with experiments [13]. Panel **d**), VHE resonant behavior in $h^{11}\text{BN}$.

i.e. $\dot{q}(\mathbf{r}, t) = \mathcal{H} \cdot [\sin(2\pi ft) + 1] \exp\left[-\frac{(x+x_c)^2}{2\sigma_x^2} - \frac{y^2}{2\sigma_y^2}\right] + \mathcal{H} \cdot [\sin(2\pi ft + \pi) + 1] \exp\left[-\frac{(x-x_c)^2}{2\sigma_x^2} - \frac{y^2}{2\sigma_y^2}\right]$. This perturbation is always non-negative, representing the laser heating employed in experiments [11–13]. Then, we monitored how the amplitude of the temperature oscillation, a , varies as a function of frequency, f . Fig. 3 shows that the solution of the periodically driven VHE in natural graphite displays resonant behavior, *i.e.* plotting the oscillation amplitude as a function of frequency, $a(f)$, we see a peak reminiscent of that observed in the frequency response of a driven underdamped oscillator. We highlight how the resonant behavior obtained from the viscous VHE is weaker than that obtained from the inviscid DPLE [56, 60, 67], while Fourier’s law does not show resonant response (analogously to an overdamped oscillator). Finally, the inset shows that reducing isotopic disorder in graphite yields a stronger VHE resonant response, and that analogous signatures are expected to emerge in $h^{11}\text{BN}$ around $T=60\text{K}$ in $15\mu\text{m}$ -long devices.

Next, we systematically investigate how the maximum resonant amplification vary as a function of device size, average temperature, and type of material. We performed simulations analogous to Fig. 3 varying device’s size [68] and equilibrium temperature, computing for every simulation the maximum resonant amplification as $\max_f[a(f)]/a_0$ (where $a_0 = \lim_{f \rightarrow 0} a(f)$, see Fig. 3). In Fig 4**a,b** we compare the inviscid DPLE (**a**) with the VHE (**b**) in natural graphite. We see that the temperatures and lengthscales at which the VHE predict the emergence of hydrodynamic resonant behavior in natural samples are in broad agreement with the temperatures and lengthscales for the emergence of heat hydrodynamics discussed by Huberman *et al.* [11]; in contrast, the DPLE fails to capture the reduction of hydrodynamic behavior as temperature is decreased below 100 K. Turning our attention to isotopically purified graphite (Fig. 4**c**),

we see that here the VHE resonant response is stronger than in natural graphite, and it also persists up to larger lengthscales and higher temperatures, in broad agreement with the experiments by Ding *et al.* [13][69]. Finally, Fig. 4**d** predicts that resonant behavior for viscous temperature waves occurs also in $h^{11}\text{BN}$, with a magnitude slightly weaker than in natural graphite.

Comparison between VHE and microscopic LBTE.— We recall that the mesoscopic VHE are obtained coarse-graining the LBTE for the microscopic phonon distribution function, and relying on homogeneous linear-response to determine the transport coefficients (*i.e.*, neglecting gradients in space and time of the out-of-equilibrium phonon distribution)[37]. Therefore, the VHE are expected to be increasingly more accurate as these gradients become weaker. To quantitatively evaluate the accuracy of the VHE at the length- and time-scales in focus here, we compare the solution of the VHE with that of the LBTE with full collision operator [70], both in the steady-state and time-dependent domain. Starting from the steady state, we show in SM V that the solution of the space-dependent LBTE in the geometry of Fig. 1 yields a temperature inversion compatible with that predicted by the VHE. Moreover, in SM VIII we show that the VHE and LBTE yield compatible predictions for the time-dependent relaxation of a micrometer-sized temperature perturbation occurring over the ~ 10 ns timescale. These analyses confirm that the length- and time-scales in focus here are sufficiently large to allow us to employ the VHE to describe heat hydrodynamics.

Conclusion.—We have shed light on the fundamental physics determining the emergence of viscous heat hydrodynamics, discussing with quantitative first-principles accuracy how to induce temperature inversion in steady-state heat vortices, and viscous temperature waves in extreme thermal conductors such as graphite and layered $h^{11}\text{BN}$. We have demonstrated that these phenomena can be amplified by engineering the device’s geome-

try, boundary conditions, or exploiting resonance, paving the way for applications in next-generation electronic and phononic technologies. We have provided novel, fundamental insights on temperature waves, showing that the viscous temperature waves emerging from the VHE differ fundamentally from the inviscid (DPLE) heat waves discussed in past works [39, 40, 56, 60, 67, 71, 72]. We have quantitatively demonstrated that viscous effects determine the hydrodynamic relaxation timescales [12] and lengthscales [11, 13] measured in pioneering experiments. These results share fundamental common underpinnings with other quasiparticle's fluid-like transport phenomena in solids—involving, e.g., electron-phonon bifluids [44, 73–79], magnons [80], skyrmions [81]—thus will potentially inspire analogous developments and applications. Finally, our findings may also directly translate to fluids flowing in porous media (relevant for e.g. soil science, hydrology, and petroleum engineering [82][83]).

ACKNOWLEDGMENTS

We thank Dr Miguel Beneitez, Dr Gareth Conduit, and Dr Orazio Scarlatella for reading and commenting the manuscript. We also gratefully acknowledge technical discussions on the BTE-barna software package with Dr Michael Rutter and Dr Martí Raya-Moreno. M. S. acknowledges support from: Gonville and Caius College; the SNSF project P500PT_203178; the Sulis Tier 2 HPC platform (funded by EPSRC Grant EP/T022108/1 and the HPC Midlands+consortium); the Kelvin2 HPC platform at the NI-HPC Centre (funded by EPSRC and jointly managed by Queen's University Belfast and Ulster University). J. D. thanks Prof Hrvoje Jasak for the hospitality in Cambridge.

SUPPLEMENTARY MATERIAL

I. DPLE AS INVISCID LIMIT OF THE VHE

In this section we show analytically that the dual-phase-lag equation (DPLE) [39, 40], widely used to describe temperature waves [56–61], emerges from the viscous heat equations (VHE) [37] in the limit of vanishing viscosity. To see this, we start from the VHE without the viscosity and source term,

$$C \frac{\partial T(\mathbf{r}, t)}{\partial t} + \alpha^{ij} \frac{\partial u^j(\mathbf{r}, t)}{\partial x^i} - \kappa^{ij} \frac{\partial^2 T(\mathbf{r}, t)}{\partial x^i \partial x^j} = 0, \quad (\text{SE } 3)$$

$$A_k \frac{\partial u_k(\mathbf{r}, t)}{\partial t} + \gamma_k^i u^i(\mathbf{r}, t) + \beta_k^i \frac{\partial T(\mathbf{r}, t)}{\partial x^i} = 0, \quad (\text{SE } 4)$$

where the indexes i, k denote Cartesian directions. Then we consider a setup where the tensors appearing in Eqs. (SE 3, SE 4) can be considered diagonal and isotropic (as is the case for a device made of graphite or h^{11}BN

with non-homogeneities exclusively in the basal plane, see Sec. IX). Thus, writing the second equation by components for the 2-dimensional case we have:

$$C \frac{\partial T}{\partial t} + \alpha \left(\frac{\partial u_x}{\partial x} + \frac{\partial u_y}{\partial y} \right) - \kappa \left(\frac{\partial^2 T}{\partial x^2} + \frac{\partial^2 T}{\partial y^2} \right) = 0, \quad (\text{SE } 5)$$

$$A \frac{\partial u_x}{\partial t} + \gamma u_x + \beta \frac{\partial T}{\partial x} = 0, \quad (\text{SE } 6)$$

$$A \frac{\partial u_y}{\partial t} + \gamma u_y + \beta \frac{\partial T}{\partial y} = 0. \quad (\text{SE } 7)$$

Differentiating both sides of Eq. (SE 6) with respect to x , and both sides of Eq. (SE 7) with respect to y , we obtain:

$$\left(A \frac{\partial}{\partial t} + \gamma \right) \frac{\partial u_x}{\partial x} = -\beta \frac{\partial^2 T}{\partial x^2}; \quad (\text{SE } 8)$$

$$\left(A \frac{\partial}{\partial t} + \gamma \right) \frac{\partial u_y}{\partial y} = -\beta \frac{\partial^2 T}{\partial y^2}. \quad (\text{SE } 9)$$

Then, we sum Eq. (SE 8) and Eq. (SE 9), obtaining:

$$\left(A \frac{\partial}{\partial t} + \gamma \right) \left(\frac{\partial u_x}{\partial x} + \frac{\partial u_y}{\partial y} \right) = -\beta \left(\frac{\partial^2 T}{\partial x^2} + \frac{\partial^2 T}{\partial y^2} \right). \quad (\text{SE } 10)$$

Now we notice that applying the operator $\hat{\mathcal{O}} = (A \frac{\partial}{\partial t} + \gamma)$ to both sides of Eq. (SE 5), and by using Eq. (SE 10), allows us to write an equation for temperature only:

$$\begin{aligned} \frac{CA}{\gamma} \frac{\partial^2 T}{\partial t^2} + C \frac{\partial T}{\partial t} - \left(\frac{\alpha\beta}{\gamma} + \kappa \right) \left(\frac{\partial^2 T}{\partial x^2} + \frac{\partial^2 T}{\partial y^2} \right) \\ - \frac{\kappa A}{\gamma} \frac{\partial}{\partial t} \left(\frac{\partial^2 T}{\partial x^2} + \frac{\partial^2 T}{\partial y^2} \right) = 0. \end{aligned} \quad (\text{SE } 11)$$

Eq. (SE 11) is exactly the DPLE equation discussed by Joseph and Preziosi [39] and Tzou [40]. We can now see the relationship between the constants appearing in the VHE, and the time lags appearing in the DPLE [40] and discussed in the main text: $\tau_T = \frac{\kappa A}{\alpha\beta + \kappa\gamma}$, $\tau_Q = \frac{A}{\gamma}$. We conclude by noting that the thermal diffusivity appearing in the DPLE is $\alpha_E = \frac{\alpha\beta + \kappa\gamma}{C\gamma}$. It can be readily seen that in the limit $\tau_T = \tau_Q$, as well as in the steady-state, the DPLE becomes equivalent to Fourier's law, while in the limit $\tau_T = 0$ it becomes equivalent to Cattaneo's second-sound equation [40].

In summary, the above derivation demonstrates that the viscous temperature waves emerging from the VHE are fundamentally different from the inviscid DPLE heat waves previously discussed in the literature [39, 40, 56, 60, 67].

II. VISCOUS HEAT BACKFLOW IN h^{11}BN

In this section we show that the emergence of heat vortices is not limited to graphite, predicting their appearance also in a device made of h^{11}BN (Fig. SF 1).

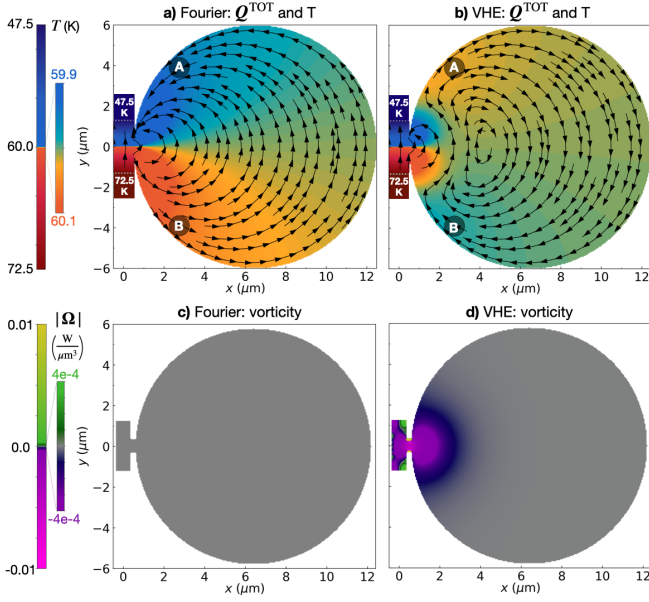


FIG. SF 1. **Signature of viscous heat backflow in $h^{11}\text{BN}$.** In-plane (x - y) heat flux (streamlines) and temperature (colormap) in a tunnel-chamber device made of $h^{11}\text{BN}$. Panel **a** (**b**) shows the solution of Fourier's equation (VHE) in the presence of a temperature gradient applied at the tunnel's boundaries (60 ± 12.5 K at $y = \pm 1.25 \mu\text{m}$), and considering the other boundaries as adiabatic (*i.e.* $\nabla T \cdot \hat{n} = 0$, where \hat{n} is the versor orthogonal to the boundary) and, in the VHE, "slipping" ($\mathbf{u} \cdot \hat{n} = 0$). In Fourier's case (**a**), the direction of the temperature gradient in the chamber mirrors that in the tunnel ($T_A < T_B$). In contrast, the VHE (**b**) account for an additional viscous component for the heat flux—not directly related to the temperature gradient, see main text—allowing the emergence of viscous backflow and temperature in the chamber reversed compared to the tunnel ($T_A > T_B$). Panel **c**), the vorticity Fourier's heat flux is trivially zero; panel **d**) shows the non-zero vorticity of the total VHE heat flux, $\nabla \times \mathbf{Q}^{\text{TOT}}$.

III. INFLUENCE OF GEOMETRY AND BOUNDARY CONDITIONS ON BACKFLOW

A. Lubrication layer and slipping boundaries

In this section we discuss the numerical techniques used to simulate different boundary conditions for the drift velocity. Specifically, in order to model boundary conditions different from no-slip ($\mathbf{u} = \mathbf{0}$ at the boundary), which correspond to boundaries that are completely dissipating the crystal momentum, we introduce a "lubrication layer", *i.e.* a region in proximity of the actual boundary in which the viscosity is greatly reduced ($\mu_{\text{lub}}^{ijkl} = \mu^{ijkl}/F$, where $F \geq 1$). By imposing a no-slip condition on the actual boundary of the device, choosing a lubrication layer width (LLW) to be small ($\lesssim 5\%$ of the device's characteristic size), and varying the factor F from 1 to an arbitrarily large number, one can mimic the effect of boundary conditions ranging from no-slip ($\mathbf{u} = \mathbf{0}$, $F=1$) to perfectly slipping ($F \rightarrow \infty$). In fact, by reducing

the viscosity in the lubrication layer, one reduces the viscous stresses due to presence of the boundary, with the limit $F=1$ representing no reduction and yielding the no-slip condition, and the limit $F \rightarrow \infty$ representing infinite reduction, *i.e.* perfectly slipping boundaries.

We show in Fig. SF 2 that, in analogy to standard fluid-dynamics, no-slip boundary conditions (panel **a**, also discussed in Ref. [37]) yield a Poiseuille-like heat-flow profile. In contrast, using slipping boundaries yield much weaker (negligible) variations of the heat-flux profile (panel **b**). The lubrication-layer approach is particularly advantageous from a numerical viewpoint. In fact, in standard solvers such as *Wolfram Mathematica*, implementing perfectly slipping boundary conditions is straightforward in simple geometries such as that in Fig. SF 2, where the Cartesian components of the drift velocity are always aligned or orthogonal to the boundaries. However, in complex geometries such as that in Fig. 1, it is not possible to find a coordinate system which is always aligned or orthogonal to the boundaries, rendering the numerical implementation of the slipping boundary conditions much more complex. We show in Fig. SF 2c) that by choosing a sufficiently small LLW ($0.1 \mu\text{m}$), and a sufficiently large value for the viscosity reduction factor ($F=10^3$), one obtains practically indistinguishable results by using the lubrication layer or the exact slipping boundary conditions. We also note that in Fig. SF 2 **a**) and **b**) the area where viscosity assumes the physical value has exactly the same size.

Thus, the test reported in Fig. SF 2 justifies the usage of the lubrication layer to simulate slipping boundary conditions in complex geometries such as the one shown in Fig. 1 [84], which we discuss in detail in the next section.

B. Tunnel-chamber geometry for viscous backflow

As mentioned in the main text, to observe steady-state hydrodynamic deviations from Fourier's law, two conditions are necessary: first, the material must have a non-negligible intrinsic thermal viscosity; second, the device's geometry and boundary conditions have to yield a significant (as large as possible) second spatial derivative of the drift velocity. Details on intrinsic material's properties are reported in Sec. IX, here we discuss how the sample's geometry and boundary conditions influence the hydrodynamic deviations from Fourier's diffusion.

We focus on materials having the same symmetries of those considered in the main text, considering in-plane transport phenomena that allow us to consider several of the tensor coefficients appearing in the VHE (1,2) as proportional to the identity: $\alpha^{ij} = \alpha \delta^{ij}$, $\kappa^{ij} = \kappa \delta^{ij}$, $\beta^{ij} = \beta \delta^{ij}$, and $\gamma^{ij} = \gamma \delta^{ij}$; see Sec. IX for details.

We start by considering a rectangular geometry with two opposite sides thermalized at different temperatures, and all the other sides adiabatic (Fig. SF 3a). In this case, the temperature gradient will be in vertical di-

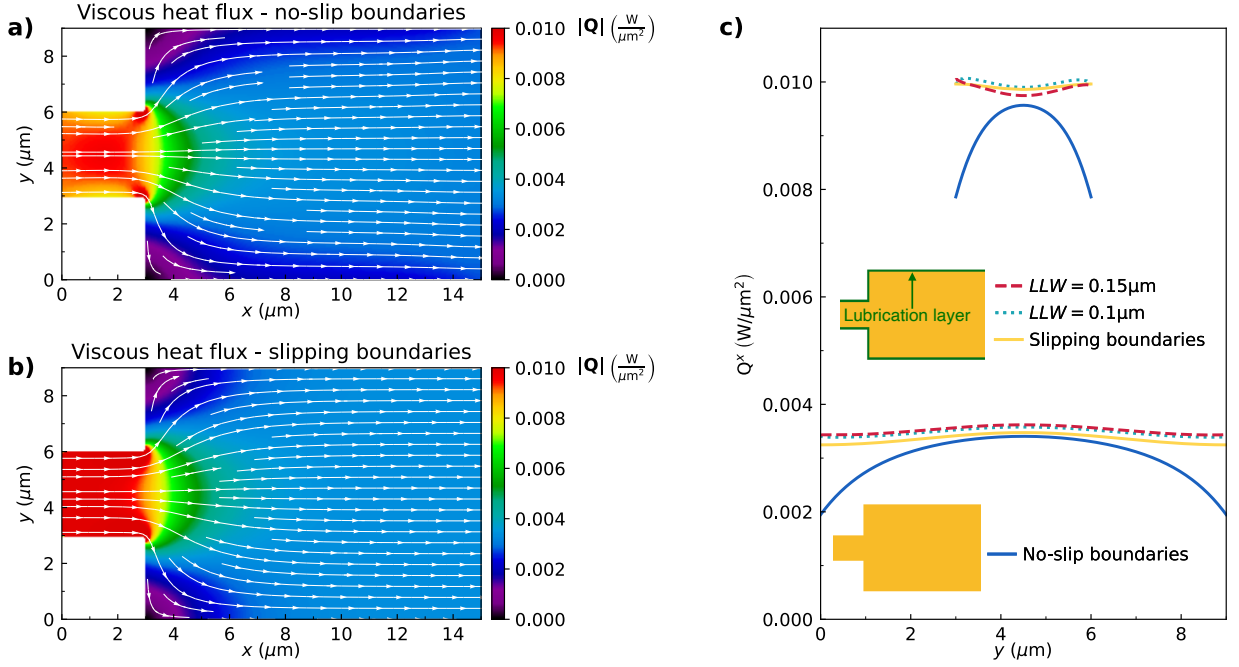


FIG. SF 2. **Effects of boundary conditions on the heat-flow profile.** In-plane (x-y) heat flow in graphite, obtained solving the VHE imposing a temperature of 80 K on the left side ($x = 0 \mu\text{m}$) and 60 K on the right side ($x = 15 \mu\text{m}$), assuming all boundaries at $x \neq 0 \mu\text{m}$ and $x \neq 15 \mu\text{m}$ to be adiabatic, and using no-slip boundary conditions for the drift velocity ($\mathbf{u} = \mathbf{0}$ at the boundary) in a) [37], and a perfectly slipping boundary condition ($\mathbf{u} \cdot \hat{\mathbf{n}} = 0$, where $\hat{\mathbf{n}}$ is the versor orthogonal to the boundary) in panel b). Panel c), differences between the heat-flow profile along the vertical sections $x = 1.5 \mu\text{m}$ and $x = 9 \mu\text{m}$ for different boundary conditions. We highlight how the lubrication-layer approach, used to model slipping boundaries in a numerically convenient way, allows to obtain results practically indistinguishable from those obtained exactly implementing the slipping boundaries. The insets in panel c) show schematically how the lubrication layer is implemented.

rection and will approximatively tend to a constant[85], and from the VHE (1,2) one can see that in the presence of slipping boundaries (*i.e.*, the only condition enforced is $\mathbf{u} \cdot \hat{\mathbf{n}} = 0$, where $\hat{\mathbf{n}}$ is the versor orthogonal to the boundary, implying no shear stress at the boundaries) this will create a drift velocity anti-aligned to the temperature gradient, $\mathbf{u} = -\frac{\beta}{\gamma} \nabla T$, thus aligned diffusive and drifting components of the heat flux ($\mathbf{Q}^\delta = -\kappa \nabla T$ and $\mathbf{Q}^D = \alpha \mathbf{u}$, respectively). If no-slip boundary conditions (corresponding to phonon-boundary scattering absorbing the phonon momentum[37, 51]) are considered in this geometry, the drift velocity is forced to assume a Poiseuille-like profile along the horizontal direction, a feature that has very small (negligible) influence on the temperature gradient along the vertical direction (see Fig. 4b of Ref. [37], and Appendix H of the same reference).

While the analysis of the perfectly rectangular geometry does not show significant deviations between Fourier and VHE, it shows that it is possible to use temperature gradients and slipping boundary conditions to generate non-zero drift velocity in proximity of boundaries. This is of practical interest. In fact, to the best of our knowledge, there are no known experimental techniques that allow to directly inject (or extract) a drift velocity in a device—for this reason all the analyses done here and in Ref. [37] consider always $\mathbf{u} = \mathbf{0}$ at boundaries in con-

tact with thermal reservoirs. The analysis here suggests that, by attaching an additional device at the slipping

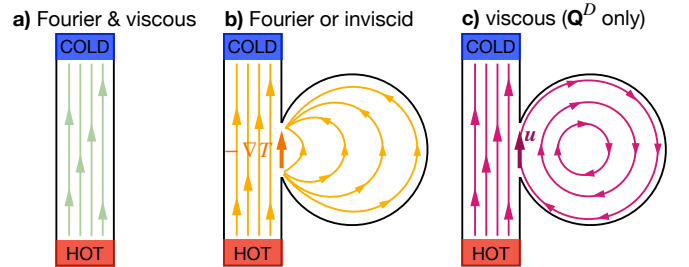


FIG. SF 3. **Representative streamlines for diffusive and viscous flow.** Panel a), illustration of streamlines emerging from Fourier or VHE in a rectangular geometry with two thermalized boundaries (T is hot (cold) in the red (blue) box, and $\mathbf{u} = \mathbf{0}$ in both boxes), and the other boundaries slipping and adiabatic. Drift-velocity and temperature-gradient component of the heat flux are aligned (green streamlines), and no significant differences are observed between VHE and Fourier. Panel b), equations for irrotational flow (Fourier or inviscid limit of the VHE) predict that a temperature gradient at the opening of a circular chamber (orange) generates dipole-like, open and counterclockwise heat-flux streamlines. Panel c), the VHE allow vortical flow and predict that, to minimize viscous stresses, the drifting heat-flux component can form closed streamlines with clockwise direction (opposite to b).

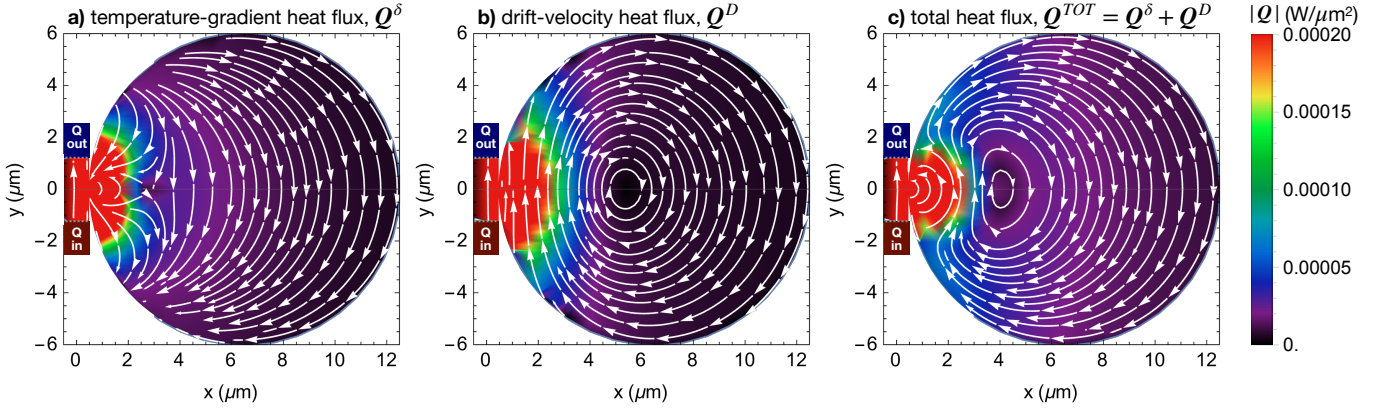


FIG. SF 4. **Heat flux in graphitic tunnel-chamber device**, obtained from the solution of the VHE. Streamlines are white, the colormap shows the magnitude of the heat flux. Panel **a**, irrotational temperature-gradient component of the heat flux, $\mathbf{Q}^\delta = -\kappa \nabla T$. Panel **b**, drifting (vortical) component of the heat flux, $\mathbf{Q}^D = \alpha \mathbf{u}$. Panel **c**, total heat flux $\mathbf{Q}^{TOT} = \mathbf{Q}^\delta + \mathbf{Q}^D$, displaying closed orbits and therefore vortical behavior. Boundary conditions are analogous to Fig. 1: a temperature gradient is present in the tunnel (70 ± 12.5 K at $y = \pm 1.25 \mu\text{m}$), and all the other boundaries are adiabatic and slipping.

boundary of the rectangular geometry, one could use the large and homogeneous (practically robust against perturbations) tunnel's drift velocity as a boundary condition to drive viscous deviations from Fourier's law in the attached device.

The most dramatic steady-state deviation from Fourier's law that we can imagine is heat backflowing from cold to hot regions. This condition emerges from the VHE when the drifting heat flux \mathbf{Q}^D has stronger magnitude and opposite direction compared to the temperature-gradient heat flux \mathbf{Q}^δ . We now elucidate how these deviations are promoted in a circular chamber having: slipping boundaries, a small opening, a small temperature gradient and constant drift velocity applied to the opening (Figs. SF 3b,c). This can be understood by noting that the irrotational form of the temperature-gradient heat flux expression ($\mathbf{Q}^\delta = -\kappa \nabla T$) implies that ∇T at the opening behaves as a the thermal counterpart of an electric dipole, *i.e.*, it generates a irrotational temperature-gradient flux with counterclockwise streamlines that never form closed paths (Fig. SF 3b). A totally analogous behavior emerges from the inviscid limit of the VHE ($\mu^{ijkl} = 0$), since in this case Eq. (2) implies $\mathbf{u} = -\frac{\beta}{\gamma} \nabla T$. Intuitively, this corresponds to having zero shear stress in the phonon fluid, allowing the drifting heat-flux component to enter into the chamber following the abrupt changes of directions imposed by the irrotational dipole-like behavior of the temperature-gradient field. In contrast, for non-negligible viscosity, when the drifting component of the heat flux changes its direction to enter into the chamber it is subject to viscous shear; to minimize such shear, it minimizes changes in its direction and thus enters into the chamber forming clockwise streamlines (Fig. SF 3c). In this regard, the slipping boundary conditions (no shear stress at the boundary, corresponding to reflective phonon-boundary scattering[51]) ensure that the drifting heat flux does not decrease in modulus as it approaches the chamber's

boundary. We also note that the VHE allows the drifting heat flux to have non-zero vorticity, which in the circular chamber geometry in focus here is evident from the formation of closed streamlines[86]. Since the total heat flux \mathbf{Q}^{TOT} is the sum of the irrotational $\mathbf{Q}^\delta = -\kappa \nabla T$ and possibly vortical $\mathbf{Q}^D = \alpha \mathbf{u}$, the streamlines of the total heat flux can be closed (Fig. SF 4). When this happens, the presence of the viscous ($\mu^{ijkl} \frac{\partial^2 u^k(\mathbf{r}, t)}{\partial r^j \partial r^l}$) and momentum-damping ($-\gamma \mathbf{u}$) terms in VHE (2), and the irrotational form of \mathbf{Q}^δ , imply that, in some parts of the \mathbf{Q}^{TOT} 's closed streamline, the temperature gradient must be aligned with the drift velocity, and in some others it must be anti-aligned—this because Stokes' theorem implies that the irrotational \mathbf{Q}^δ must have zero circulation on the closed streamline. As mentioned before, anti-aligned behavior emerges in the diffusive or inviscid limit, where $\mathbf{u} = -\frac{\beta}{\gamma} \nabla T$, and Eq. (2) shows that aligned behavior requires viscous effects to dominate over momentum dissipation ($|\mu^{ijkl} \frac{\partial^2 u^k(\mathbf{r}, t)}{\partial r^j \partial r^l}| \gg |\gamma^{ij} u^j(\mathbf{r}, t)|$); this permits the emergence of the viscous temperature inversion observed in Fig. 1b [87]. This illustrative analysis is quantitatively confirmed in Fig. SF 4, where we show that in the tunnel-chamber geometry of Fig. 1 the temperature-gradient flux does not form closed streamlines, while the drifting velocity does, and the total, irrotational heat flux shows indeed closed streamlines.

In summary, the tunnel-chamber geometry allows to have boundary conditions at the opening of the chamber that are antithetical for the two components of the VHE heat flow: the temperature dipole at the opening drives a heat flux with open streamlines and in counterclockwise direction in the chamber; in contrast, the large non-zero drift velocity at the opening drives drifting heat-flux streamlines that tend to be closed and in clockwise direction. The relative strength of these two heat-flux components is affected by device's geometrical properties such as diameter of the chamber as well as the

size of the opening. The former is analyzed in detail in Fig. SF 7; the latter directly influences the strength of the dipole-like temperature gradient field, as well as shear stress applied by the boundary drift velocity to the \mathbf{u} field inside the chamber. We have verified numerically that using increasingly larger openings yields stronger dipole-like temperature-gradient fields, which hinder viscous backflow. In this work the size of the opening has been fixed to $0.52 \mu\text{m}$ (see Fig. SF 5), such value is sufficiently small to yield visible effects of viscous heat backflow, and sufficiently large to be within the regime in which LBTE and VHE yield overall compatible predictions (see Fig. SF 8).

C. Slipping boundaries and heat vortices

After having shown in Sec. III A that the lubrication layer allows to model boundary conditions for the drift velocity ranging from no-slip to perfectly slipping, we use this approach to study how the inversion of the temperature gradient observed in Fig. 1 depends on the boundary conditions (Fig. SF 5).

To understand how the smoothness of the device's boundaries (*i.e.*, their capability to reflect phonons [51]) affects the magnitude of the temperature inversion, we analyze how the temperature difference between the two representative points A and B in Fig. 1, $\Delta T_{AB} = T_A - T_B$, depends on the viscosity reduction factor F

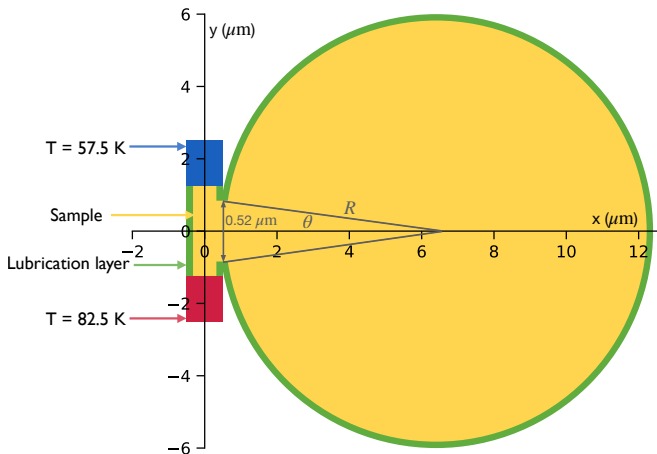


FIG. SF 5. **Tunnel-chamber geometry for observation of steady-state viscous heat backflow.** The yellow region is the simulation domain where all the parameters entering in the VHE assume physical values; the green area is the lubrication-layer region, where the viscosity is reduced by a factor F to account for partially reflective boundaries. The width of the lubrication layer ($0.1 \mu\text{m}$), and of the opening connecting the tunnel and the chamber ($0.52 \mu\text{m}$), are represented in an exaggerated way for graphical clarity. The opening angle used here and in Fig. 1 is $\theta = 4.9672^\circ$. A temperature of 82.5 K (57.5 K) is applied at the lower (upper) opening of the tunnel, all the other boundaries are adiabatic.

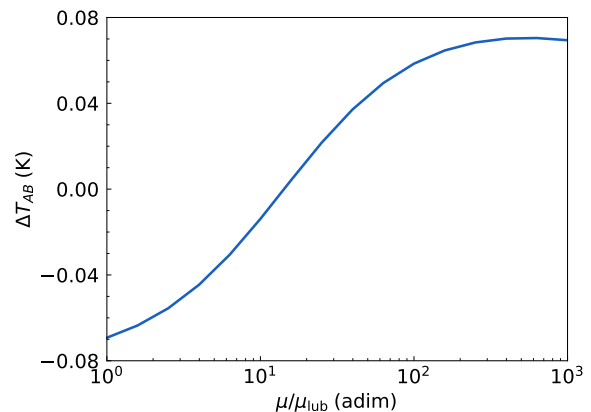


FIG. SF 6. **Dependence of the temperature inversion due to viscous backflow on the boundary conditions.** We plot the temperature difference $\Delta T_{AB} = T_A - T_B$, measured in the spots A and B of the natural-graphite device of Fig. 1 as a function of the reduction of viscosity in the lubrication layer with $\text{LLW} = 0.1 \mu\text{m}$. $\mu/\mu_{\text{lub}} = 1$ corresponds to no-slip boundaries; $\mu/\mu_{\text{lub}} = 10^3$ practically corresponds to perfectly slipping boundaries.

used in the lubrication layer. We recall from Fig. SF 2 that $F = 1$ corresponds to no-slip, phonon-absorbing boundaries, while large $F = 10^3$ corresponds to slipping, phonon-reflective boundaries. A positive difference $\Delta T_{AB} > 0$ is observed when viscous heat backflow causes a behavior analogous to Fig. 1b, while $\Delta T_{AB} < 0$ is obtained when the system overall behaves analogously to Fourier's law (Fig. 1a). We show in Fig. SF 6 how ΔT_{AB} changes as a function of the viscosity reduction in the lubrication layer. We see that as the viscosity in the lubrication layer is reduced, ΔT_{AB} switches from negative (Fourier-like) to positive (vortex-like), indicating that (at least partially) slipping boundaries are needed to observe the temperature inversion related to viscous heat backflow. We highlight how, in the limit of vanishingly low viscosity for the lubrication layer, the temperature inversion ΔT_{AB} converges to a constant, confirming that the viscosity in the lubrication layer is so reduced that the overall effect is that of perfectly slipping boundaries.

In summary, the results in Fig. SF 6 suggest that smooth, phonon-reflective boundaries are needed to observe heat vortices and related temperature inversion, and conversely measurements of hydrodynamic heat transport may be used to characterize the roughness of devices' boundaries, *i.e.* their capability to reflect phonon's crystal momentum[51].

IV. EFFECTS OF TEMPERATURE, SIZE, AND ISOTOPES ON VISCOUS HEAT BACKFLOW

In this section we explore how the temperature inversion due to viscous heat backflow depends on the size of the device, the average temperature around which the temperature gradient is applied, and the presence of

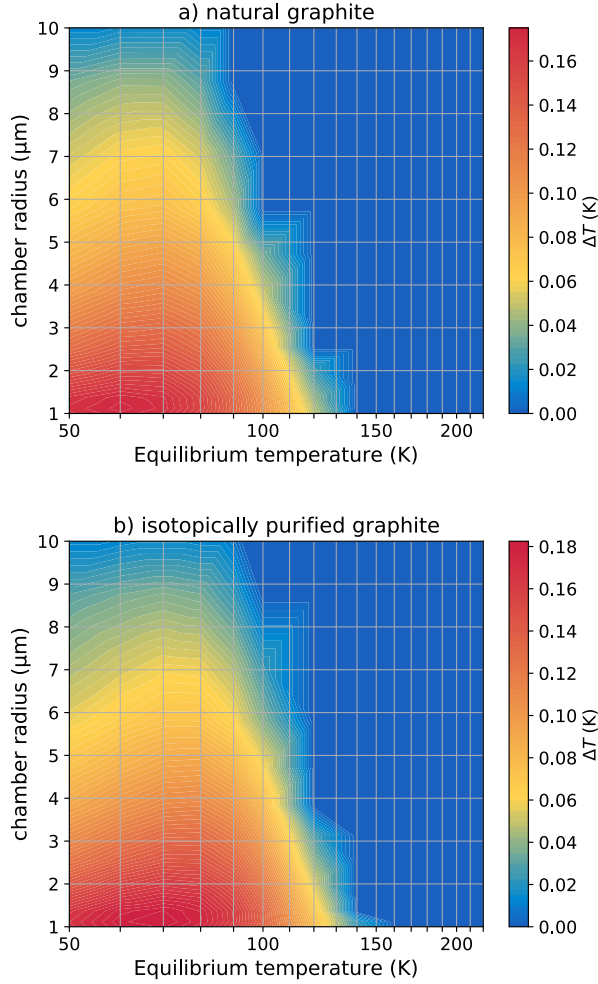


FIG. SF 7. **Effects of temperature, size, and isotopic disorder on viscous heat backflow.** The colormap shows how the temperature inversion due to viscous backflow, computed as the difference between the maximum temperature in the upper part of the chamber ($y > 0$) and the minimum temperature in the lower part in the chamber ($y < 0$), depends on the radius of the chamber and on the average temperature \bar{T} of the tunnel (a perturbation of $\delta T = \bar{T} \pm 12.5 K$ is always used at the extremities of the tunnel). Panel **a**) refers to samples with natural-abundance isotopic disorder, while panel **b**) shows isotopically purified samples.

isotopic-mass disorder in graphite (this latter affects the parameters such as intrinsic thermal conductivity and intrinsic thermal viscosity of the sample). We show in SF 7 that the temperature inversion due to viscous heat backflow is maximized at average temperatures below 100 K for natural graphite (98.9 % ^{12}C , 1.1 % ^{13}C) and below 110 K for isotopically purified graphite (99.9 % ^{12}C , 0.1 % ^{13}C). Moreover, the temperature inversion is not significantly affected by the chamber's radius, and it is slightly larger in isotopically purified samples compared to natural samples. We note finite-size effects on the parameters entering in the VHE have been taken into account following the approach detailed in Ref. [37] and considering a grain size equal to the diameter of the chamber.

V. STEADY-STATE VISCOUS HEAT BACKFLOW FROM THE LBTE

In this section we solve the space-dependent Linearized phonon Boltzmann Transport Equation (LBTE) with full scattering operator in the tunnel-chamber geometry of Fig. SF 8. We rely on the deviational Monte Carlo solver provided in the **BTE-Barna** software package[70], computing the scattering operator in the three-dimensional Brillouin zone of graphite, and simulating a device extremely long in the off-plane direction (*i.e.*, with transport taking place in-plane and with temperature and heat flux depending only on the in-plane coordinates x, y), as in Fig 1. Computational details are reported in Sec. V A.

Fig. SF 8a shows that the viscous temperature inversion predicted by the VHE around $\bar{T} = 70$ K (Fig. 1b) emerges also from the space-dependent solution of the LBTE with full collision matrix. The LBTE is solved starting from a uniform temperature $T(x, y) = \bar{T}$ in the devices' interior and applying a temperature difference of 25 K at the boundaries of the tunnel (*i.e.*, 82.5 K at the tunnel's boundary at $y = -1.25\mu\text{m}$, and 57.5 K at $y = 1.25\mu\text{m}$). As time evolves, heat flows into the tunnel and enters into the chamber, and the temperature profile evolves towards the steady state (Fig. SF 8b shows that the system is practically in the steady state at $t \gtrsim 6$ ns). We highlight how, at the steady state, the magnitude of the temperature inversion emerging from the LBTE is compatible with that emerging from the VHE in Fig 1b. Additionally, we note that in proximity of the chamber's opening, where non-homogeneities in the geometry and heat flux are maximized, differences between the solution of the LBTE and VHE are visible in temperature and heat flux; these might originate from discarding spatial gradients of the out-of-equilibrium phonon distribution when coarse-graining the LBTE into the VHE[37]. Nevertheless, we note that these differences have practically negligible effect on the temperature inversion observed far from the opening (Fig. SF 8b) and as such are unimportant for the scope of the present work.

It is worth mentioning that the temperature difference of 25 K applied at the tunnel's boundaries has been chosen as a trade-off between the following two requirements: first, in the device the temperature deviations from equilibrium must be small enough to remain in the regime of applicability of the LBTE (either for evaluating its space-dependent solution[70], or for coarse-graining it into the VHE[37]); second, the temperature deviation (gradient) must be sufficiently large to generate a significant vortical heat flux at the entrance of the tunnel. We recall that here the tunnel is used to generate conditions at the chamber's opening suitable to observe hydrodynamic deviations from Fourier's law (Sec. III B); inside the chamber (where backflow and temperature inversion occur) the temperature deviations are about 2‰ of the average temperature, as such the LBTE is expected to be particularly accurate inside the chamber.

We also note that the space-dependent heat flux and

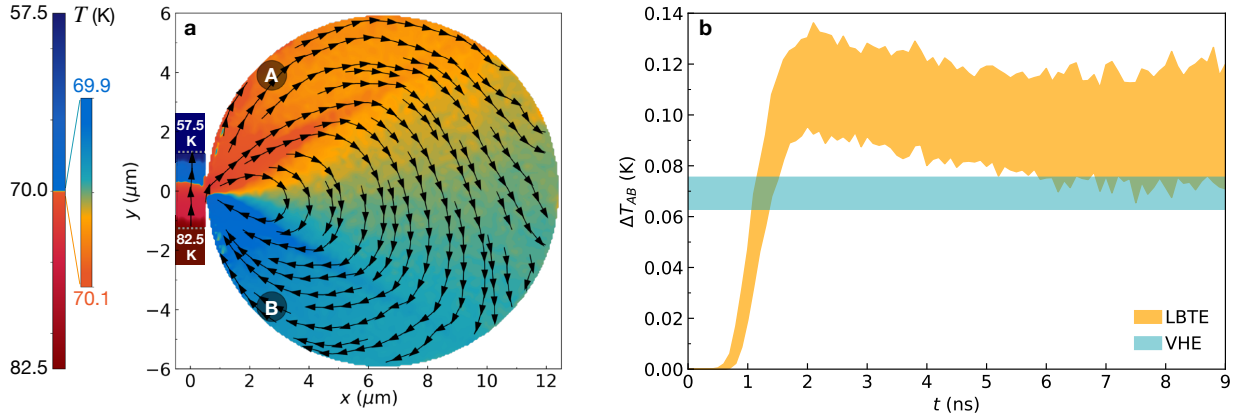


FIG. SF 8. **Viscous heat backflow and temperature inversion from the space-dependent solution of the LBTE.** Panel a), temperature field (colormap) and total in-plane heat flux (streamlines) obtained from the solution of the full LBTE for a tunnel-chamber device, made of natural graphite and at an average temperature of $\bar{T} = 70$ K. Two thermal reservoirs are applied at the tunnel’s boundaries (at $y = \pm 1.25 \mu\text{m}$ temperature is fixed to $T = \bar{T} \mp 12.5$ K), the other boundaries are adiabatic and slipping. Panel b), time evolution of ΔT_{AB} —the orange area shows the maximum temperature in the spot A minus the minimum temperature in the spot B, both having diameter $1 \mu\text{m}$ —as the LBTE solution equilibrates towards the steady state (see text); the blue region shows the ΔT_{AB} obtained from the steady-state solution of the VHE in the same device (Fig. 1b).

temperature in Fig. SF 8 are obtained integrating the microscopic deviational heat flux and energy density, which are both related to the phonon distribution that solves the LBTE, see Ref. [88] and Eqs. (6) and (7) in Ref. [70]. As discussed in Ref. [89], temperature and heat flux are well defined within the LBTE with full, energy-conserving collision operator and in the presence of heaters or thermal reservoirs that specify temperature at the boundaries. In particular, the definition of a mesoscopic, space-dependent temperature is related to the constraint of conservation of energy in microscopic phonon collisions—formally this derives from the fact that phonon distributions $n(\mathbf{q}, \mathbf{r})_s$ (where \mathbf{q} , s , and \mathbf{r} are the wavevector, mode index, and position of the phonon wavepacket, respectively) proportional to the phonon energies $\hbar\omega(\mathbf{q})_s$ are eigenvectors with zero eigenvalue of the full collision matrix appearing in the LBTE [89, 90]. We note that the temperature appearing in the VHE directly follows from the microscopic energy conservation within the exact LBTE, as it is obtained projecting the LBTE into the subspace of the eigenvector with zero eigenvalue proportional to the phonon energies[37].

It is important to note that a non-homogeneous, space-dependent temperature is necessary to have heat transport in our setup (Fig. SF 5). Specifically, we recall that we always consider $\mathbf{u} = \mathbf{0}$ at non-adiabatic boundaries in contact with thermal reservoirs, since we are not aware about any experimental technique that allows to directly inject a drift velocity in a device. Under these conditions, non-homogeneities that drive heat transport can be introduced exclusively via thermal reservoirs at different temperature; these imply a non-zero temperature gradient (*i.e.*, heat flux \mathbf{Q}^δ), which then generates drift velocity (*i.e.*, heat flux \mathbf{Q}^D) via the coupling between ∇T and \mathbf{u} appearing in Eq. 2.

Overall, the analyses in this section confirm that the

size of the device in Fig. 1 is sufficiently large for the VHE to be accurate enough to describe the viscous heat backflow and temperature inversion that emerge from the solution of the full, space-dependent LBTE. It is also worth mentioning that the mesoscopic description of the hydrodynamic viscous heat backflow provided by the VHE has a computational cost that is more than two order of magnitude lower than that needed to solve the LBTE[91].

A. Computational details of LBTE simulation

To convert the harmonic and anharmonic force constants from Quantum ESPRESSO/D3Q format[92, 93] we proceeded as follows. We used the Phonopy code[94, 95] to parse the harmonic force constants from Quantum ESPRESSO to FORCE_CONSTANTS format, which is readable by the LBTE solver BTE-Barna[70]. We have then inverted the code `import_shengbte` from the D3Q/thermal2 package[96] to convert the third-order anharmonic force constants from Quantum ESPRESSO-D3Q to ShengBTE[97] format, since the latter is readable by BTE-Barna[70]. We implemented the slipping boundary conditions following Sec. 4.2.2.1. ‘Specular scattering’ of Ref. [98] (such development will be made publicly available in a next release of BTE-Barna). The collision matrix was computed using a $17 \times 17 \times 3$ mesh, using the adaptive smearing and a `scalebroad` parameter[97] equal to 0.1, and accounting for isotopic scattering[99] at natural abundance (98.9 % ^{12}C and 1.1 % ^{13}C). These parameters correspond to the highest accuracy with which the space-dependent solution of the LBTE can be evaluated with the computational resources at our disposal. Using these parameters in the much less expensive calculation of the homogeneous (bulk) in-plane conductivity with the iterative method in BTE-Barna[70]

yields $\kappa(17 \times 17 \times 3, 70K) = 4482.89$ W/mK, a value that is compatible within 15% with the computationally converged bulk conductivity reported in Tab. I of Ref. [37], $\kappa(49 \times 49 \times 3, 70K) = 5302.27$ W/mK (the latter was computed with the exact diagonalization ‘relaxon’ method). The space-dependent solution of the LBTE was determined in a device ideally very long in the off-plane direction and with transport depending only on the in-plane coordinates (x, y) , *i.e.* under the hypothesis adopted also in Fig 1. In practice, such condition corresponds to considering that the device’s aspect ratio is such that the phonon distribution function entering in the LBTE is independent from the off-plane (z) direction.

VI. BOUNDARY CONDITIONS FOR TIME-DEPENDENT SIMULATIONS

A. Thermalisation lengthscale

In actual experimental devices thermalisation is not perfectly localized in space, but occurs over a finite lengthscale [48], *i.e.* there is a smooth transition from the device interior to the thermal bath. Therefore, we model the boundaries relying on a compact sigmoid function [100] to smoothly connect the a thermal bath region, where temperature is fixed and drift velocity is zero (since

at equilibrium phonons are distributed according to the Bose-Einstein distribution, which has zero drift velocity [37]), and the device’s interior, where the evolution of temperature and drift velocity is governed by the viscous heat equations. Specifically, we used the smooth-step function [101] that is ubiquitously employed in numerical calculations, *i.e.* a sigmoid Hermite interpolation between 0 and 1 of a polynomial of order 5:

$$f(r) = \begin{cases} 0, & \text{if } d(r) < 0 \\ 1, & \text{if } d(r) > 1 \\ 6[d(r)]^5 - 15[d(r)]^4 + 10[d(r)]^3, & \text{otherwise} \end{cases} \quad (\text{SE } 12)$$

where $d(r) = \left(\frac{r - R_{\text{in}}}{R_{\text{out}} - R_{\text{in}}} \right)$ and $r > 0$, as well as $R_{\text{in}} > 0$ and $R_{\text{out}} > 0$. The function is second order continuous and saturates exactly to zero and one at the points R_{in} and R_{out} , respectively. We show in Fig. SF 9 the sigmoid function (SE 12) for $R_{\text{in}} = 10 \mu\text{m}$ and R_{out} ranging from 11 to 20 μm : $R_{\text{out}} \simeq R_{\text{in}}$ simulates an ideal thermalisation (occurring over a negligible lengthscale), while $R_{\text{out}} \gg R_{\text{in}}$ simulates a very inefficient (non-ideal) thermalisation that occurs over a very large lengthscale. Then, relying on the sigmoid (SE 12) we connected smoothly the thermal bath region, where $f(\mathbf{r}) = 1$, $T(\mathbf{r}, t) = \bar{T}$, and $\mathbf{u}(\mathbf{r}, t) = \mathbf{0}$, with the device’s interior region, where $f(\mathbf{r}) = 0$ and the evolution of $T(\mathbf{r}, t)$ and $\mathbf{u}(\mathbf{r}, t)$ is governed by the VHE. In formulas, we have that

$$f(\mathbf{r})[T(\mathbf{r}, t) - \bar{T}] + [1 - f(\mathbf{r})] \left(C \frac{\partial T(\mathbf{r}, t)}{\partial t} + \alpha^{ij} \frac{\partial u^j(\mathbf{r}, t)}{\partial r^i} - \kappa^{ij} \frac{\partial^2 T(\mathbf{r}, t)}{\partial r^i \partial r^j} - \dot{q}(\mathbf{r}, t) \right) = 0, \quad (\text{SE } 13)$$

$$f(\mathbf{r})u^i(\mathbf{r}, t) + [1 - f(\mathbf{r})] \left(A^{ij} \frac{\partial u^j(\mathbf{r}, t)}{\partial t} + \beta^{ij} \frac{\partial T(\mathbf{r}, t)}{\partial r^j} - \mu^{ijkl} \frac{\partial^2 u^k(\mathbf{r}, t)}{\partial r^j \partial r^l} + \gamma^{ij} u^j(\mathbf{r}, t) \right) = 0. \quad (\text{SE } 14)$$

Details on how the non-ideal thermalisation affects the magnitude of signatures of heat hydrodynamics are reported later in this document.

B. Modeling realistic thermalisation in a rectangular geometry

In order to apply the realistic-thermalisation boundary conditions discussed in Sec. VIA to the rectangular device of Fig. 2, we employed a smoothed rectangular domain, since we noted that smooth simulation domains yielded better computational performances (faster convergence with respect to the discretization mesh, reduced numerical noise) compared to non-smoothed rectangular domains. The equation defining the smoothed rectangular-

lar domain employed in Figs. 2,3,4 is:

$$\left(\frac{|x|}{a_{\text{out}}} \right)^{\frac{2a_{\text{out}}}{\lambda}} + \left(\frac{|y|}{b_{\text{out}}} \right)^{\frac{2b_{\text{out}}}{\lambda}} = 1, \quad (\text{SE } 15)$$

where a_{out} and b_{out} are the sides of the rectangular domain where the thermalisation is perfect (outside the dashed-lime region in Fig. SF 10); λ controls the smoothness of the corners, and we used $\lambda = \frac{a_{\text{out}}}{3}$ to obtain a domain smooth enough for numerical purposes and sharp enough to practically model a rectangular device. We note that the sigmoid function (SE 12) has to be adapted to be employed in a rectangular geometry. Specifically, in Eq. (SE 12) in place of the distance r we used a distance of the form

$$\tilde{r}(x, y) = \left[\left(\frac{|x|}{a_{\text{out}}} \right)^{\frac{2a_{\text{out}}}{\lambda}} + \left(\frac{|y|}{b_{\text{out}}} \right)^{\frac{2b_{\text{out}}}{\lambda}} \right]^{1/p}, \quad (\text{SE } 16)$$

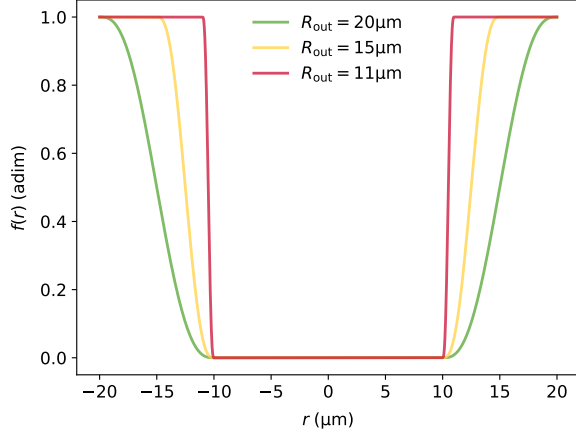


FIG. SF 9. **Sigmoid function to model realistic thermalisation.** The sigmoid function (SE 12) is plotted for $R_{in} = 10\mu m$ and various values of R_{out} . $R_{out} = 11\mu m$ (red) simulates a nearly ideal thermalisation (*i.e.*, occurring over a very short lengthscale), $R_{out} = 15\mu m$ (orange) is an estimate of a realistic thermalisation length [48], and $R_{out} = 20\mu m$ (green) represents a less efficient thermalisation.

where p controls the nonlinearity in which the two terms in Eq. (SE 16) are combined, and we chose $p = 20$ (this value will be justified later). Then, the distance (SE 16) is nested into the function $d(\tilde{r}) = \left(\frac{\tilde{r}(x,y) - R_{in}}{R_{out} - R_{in}} \right)$. It is evident that $d(\tilde{r}) < 0$ when $\tilde{r}(x,y) < R_{in}$, and $d(\tilde{r}) > 1$ when $\tilde{r}(x,y) > R_{out}$. Therefore, if one sets $R_{in} = \tilde{r}(a_{in}, b_{in})$, and $R_{out} = \tilde{r}(a_{out}, b_{out})$, and inserts $d(\tilde{r})$ into Eq. (SE 12), the resulting function $f[d(\tilde{r})]$ is exactly zero inside the rectangle having sides a_{in}, b_{in} (red region in Fig. SF 10, where the evolution of temperature and drift velocity is determined by the VHE) and exactly one outside the rectangle having side a_{out}, b_{out} (green region in Fig. SF 10, where

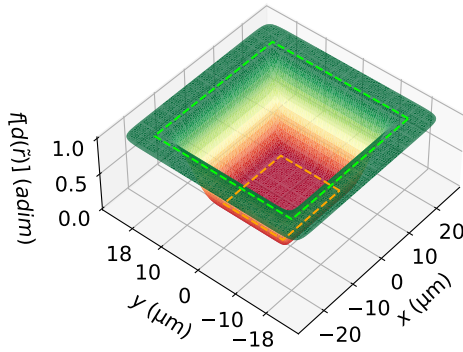


FIG. SF 10. **Sigmoid function to model realistic thermalisation in rectangular geometry.** Green (outside the dashed-line line) is the perfectly thermalised region, where the sigmoid function $f(d(\tilde{r}))=1$, and the thermal reservoir ensures that temperature is perfectly constant and the drift velocity is zero. Red (inside the dashed-orange line) represents the inner "free" region where $f[d(\tilde{r})]=0$ and the evolution of T and \mathbf{u} is determined by the VHE.

the thermal reservoir ensures that temperature is perfectly constant and the drift velocity is zero). The value of p in Eq. (SE 16) affects how the sigmoid function goes from zero to one between the dashed-orange and dashed-green rectangles, and the aforementioned value $p = 20$ was chosen after checking that the overall transition was sufficiently smooth for numerical purposes (Fig. SF 10). In the next section we investigate how the thermalisation lengthscale, $a_{out} - a_{in}$, affects lattice cooling (this investigation will be done varying only a_{out}, b_{out} in the above equations and keeping all the other parameters fixed).

C. Dependence of VHE lattice cooling on the boundary conditions

In this section we investigate how the magnitude of the viscous temperature oscillations discussed in Fig. 2 depends on the thermalisation lengthscale at the boundaries. In order to quantify the magnitude of temperature oscillations, we define a descriptor to capture the "lattice cooling strength" (LCS)

$$LCS = \frac{\bar{T} - T_{\min}}{T_{\max} - T_{\min}}, \quad (\text{SE } 17)$$

where $T_{\max} = \max_t[T(\mathbf{r}_c, t)]$ and $T_{\min} = \min_t[T(\mathbf{r}_c, t)]$ are the maximum and minimum temperatures, respectively, observed during the relaxation in the point $\mathbf{r}_c = (x_c, 0)$, where the perturbation

$$\dot{q}(\mathbf{r}, t) = \mathcal{H} \theta(t_{\text{heat}} - t) \exp \left[-\frac{(x+x_c)^2}{2\sigma_x^2} - \frac{y^2}{2\sigma_y^2} \right] \quad (\text{SE } 18)$$

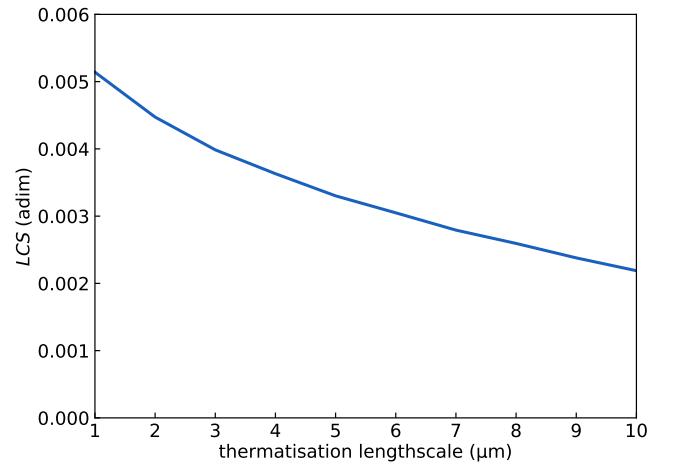


FIG. SF 11. **Dependence of lattice cooling strength on the thermalisation lengthscale.** We show how LCS in a device having non-thermalised region equal to $20\mu m \times 16\mu m$ (as in Fig. 2) depends on the thermalisation lengthscale, *i.e.* the length over which the sigmoid function shown in Fig. SF 9 goes from zero to one. Even if LCS decreases as the thermalisation lengthscale increases, LCS remains appreciable even at thermalisation lengthscales as large as $10\mu m$.

is centered. We recall that we used $\mathcal{H} = 0.013 \frac{W}{\mu m^3}$, $t_{\text{heat}} = 0.4 ns$, $x_c = 5 \mu m$, $\sigma_x = 2 \mu m$, $\sigma_y = 2.8 \mu m$, to ensure that the perturbation created causes variations within 10% of the equilibrium temperature ($\bar{T} = 80 K$). Clearly, LCS is zero if lattice cooling does not take place, and assumes a positive value if lattice cooling occurs. To gain insights on how lattice cooling (transient heat back-flow) is affected by the thermalisation lengthscale, we fixed the size of the non-thermalised region (where the sigmoid function (SE 12) is zero) to $20 \mu m \times 16 \mu m$ (*i.e.* exactly as in Fig. 2), thus we tested how the LCS emerging from the VHE varies by thermalising the boundaries with a different lengthscale, as discussed in Sec. VIA. We show in Fig. SF 11 that LCS assumes smaller values as the thermalisation becomes weaker. We highlight how lattice cooling is visible for thermalisation lengthscales as large as $10 \mu m$ (equal to half the size of the simulated device). In Figs. 2, SF 13, SF 14, and in the following, we use a thermalisation lengthscale of $2 \mu m$, a value that is expected to be a realistic representation of experimental conditions [48].

D. Effects of isotopic disorder, average temperature, and size on VHE lattice cooling

In this section we discuss how isotopic-mass disorder, size of the sample, and temperature affect the LCS emerging from the VHE in graphite. The effect of isotopic-mass disorder is taken into account by the parameters appearing in the VHE. These were computed from first principles for graphite with natural concentration of isotopes (98.9% ^{12}C , 1.1% ^{13}C) and for isotopically purified samples (99.9% ^{12}C , 0.1% ^{13}C), see Sec. IX for details. The effect of sample size was considered by uniformly rescaling the simulation domain (SE 15) and the perturbation (SE 18). We accounted for grain-boundary scattering as discussed in Ref. [37], considering a grain size of $20 \mu m$ that is realistic for high-quality samples [12, 13]. The temperature was monitored in the same point where the perturbation was applied. The effect of equilibrium temperature was taken into account through the temperature dependence of the parameters entering in the viscous heat equations, as shown by Table I in Ref. [37] and Table. I at the end of this manuscript.

We show in Fig. SF 12 that in natural samples lattice cooling is maximized at temperatures around 70-120 K and is significant in devices having size 5-20 μm . Importantly, LCS becomes negligible in devices having size larger than 30 μm . We note that Ref. [12] performed pump-probe experiments in graphite using heaters with radius equal to $6 \mu m$ (details are reported in the Supplementary Material of that reference). When we used a simulation setup similar to the experiments of Ref. [12], *i.e.* $\sigma_x = 6 \mu m$ in Eq. (SE 18) and simulation boundaries separated by a large distance (80 μm), we did not find temperature oscillations (LCS=0 in the point highlighted with the white cross in the upper panel of Fig. SF 12),

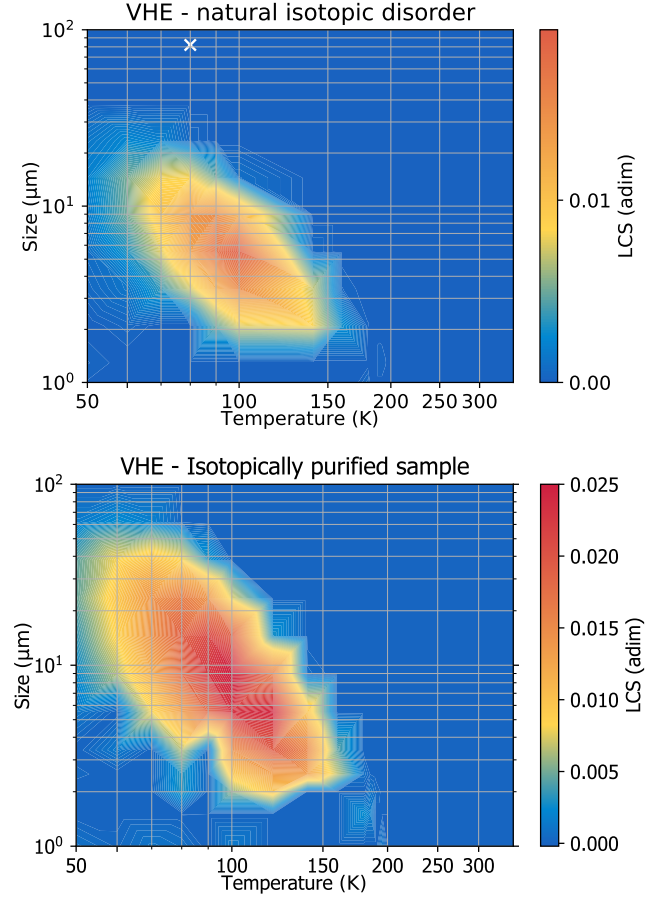


FIG. SF 12. **Lattice cooling strength as a function of size, temperature, and isotopic disorder.** The lattice cooling strength (SE 17) is reported as a function of the characteristic size of the rectangle and equilibrium temperature around which the perturbation is applied. The white cross in the upper panel represent the simulation conditions which are closest to the single-spot experiments discussed in Sec. 3 of the Supplementary Material of Ref. [12]—the lack of lattice cooling predicted under these conditions agrees with the experiments. We note that lattice cooling in natural samples (upper panel) is weaker compared to isotopically purified samples (bottom panel).

in agreement with the experiments of Ref. [12]. We also simulated the ring-shaped geometry used by Jeong *et al.* [12]: in Sec. VIII we show that the solution of the VHE in such geometry is in agreement with the corresponding LBTE solution discussed in Ref. [12] (also in agreement with experiments reported in the same reference).

VII. COMPARISON BETWEEN VISCOUS, INVISCID, AND DIFFUSIVE RELAXATIONS

A. Inviscid (DPLE) relaxation

In this section we discuss how the thermal viscosity affects temperature oscillations. Fig. SF 13 shows that solving the viscous heat equations in the inviscid limit ($\mu = 0$)—which is analytically equivalent to solving the DPLE equation, see Sec. I—yields temperature oscillations with a higher magnitude compared to those obtained in the case of the viscous heat equations (Fig. 2). Therefore, Fig. SF 13 shows that a finite viscosity is not necessary to observe lattice cooling, since a lagged response between temperature gradient and heat flux can emerge also in the inviscid limit, as detailed in Sec. I. However, we will show later in Sec. VIII that accounting for the thermal viscosity is necessary to reproduce the relaxation emerging from the time-dependent solution of the microscopic LBTE. Fig. 4 in the main text discusses how accounting for thermal viscosity is necessary to describe the lengthscales at which Huberman *et al.* [11] and Ding *et al.* [13] observed hydrodynamic behavior.

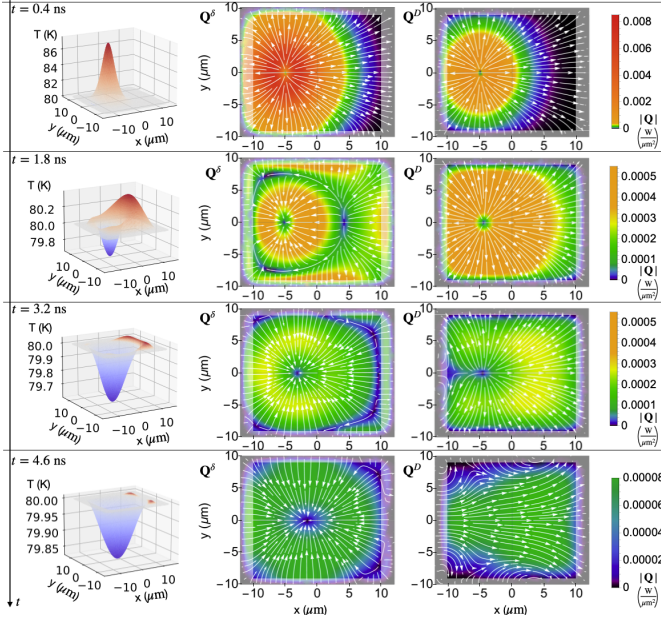


FIG. SF 13. **Transient hydrodynamic heat backflow and lattice cooling in the DPLE (inviscid) limit.** We show the DPLE predictions for the relaxation in time of a temperature perturbation (obtained applying a localized heater to a device in the time interval from 0 to 0.4 ns) in a graphitic device thermalised at 80 K the boundaries (thermalisation occurs in shaded regions, see SM VIA). Rows show different instants in time for temperature (left column), temperature-gradient heat-flux component (Q^δ , central column), and drifting heat-flux component (Q^D , right column). The emergence of lattice cooling, *i.e.* a temperature locally and transiently lower than the initial value $T=80$ K, is evident and originates from the lagged coupled evolution of Q^δ and Q^D .

B. Diffusive (Fourier) relaxation

We show in Fig. SF 14 that temperature oscillations do not emerge from Fourier's law. This behavior was trivially expected from an analytical analysis of Fourier's diffusive equation, $C \frac{\partial T}{\partial t} - \kappa^{ij} \frac{\partial^2 T}{\partial r^i \partial r^j} = 0$, whose smoothing property [64] implies that the evolution of a positive temperature perturbation relaxes to equilibrium decaying in a monotonic way. Also, within Fourier's law the heat flux has one single component proportional to the temperature gradient, so heat backflow is impossible.

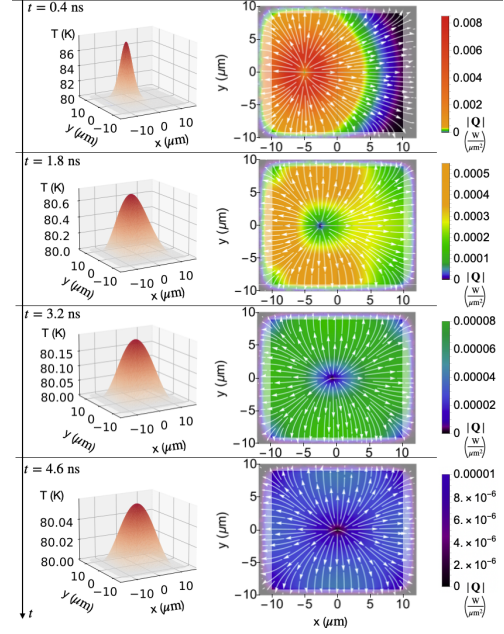


FIG. SF 14. **Temporal evolution of a localized temperature perturbation according to Fourier's law.** Rows show different instants in time for the temperature profile (left) and heat flux (right).

C. Comparing VHE, DPLE & Fourier's relaxations

The device geometry, the transient perturbation, and the boundary conditions used in Figs. 2, SF 13, SF 14 are exactly the same. In Fig. SF 15, we compare the predictions from the viscous VHE, the inviscid DPLE, and the diffusive Fourier's law for the evolution in time of the temperature in the point $r_c = (5\mu m, 0\mu m)$, where the temperature perturbation is centered. We see that both DPLE and VHE yield a wave-like relaxation for temperature, the inviscid (DPLE) relaxation is faster and yields stronger oscillatory behavior compared to the VHE relaxation. In contrast, an oscillatory relaxation for temperature is absent in Fourier's law.

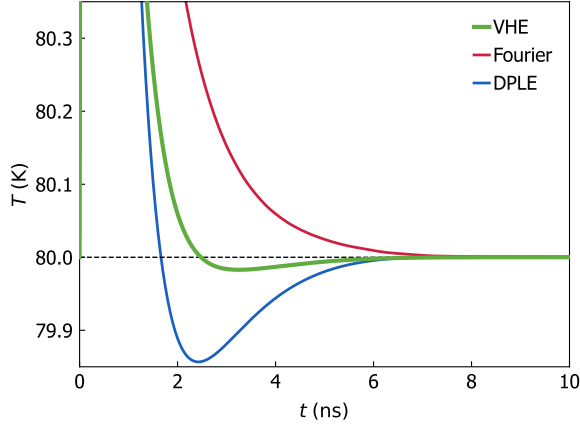


FIG. SF 15. **Temperature relaxation from VHE, DPLe, and Fourier's law.** The temporal evolution of the temperature in the center ($5\mu\text{m}, 0\mu\text{m}$) of the external heat source (switched off at $t=0.4$ ns, see text for details) is shown in red for Fourier's law, in blue for the DPLe, and in green for the VHE. Temperature oscillations are visible both in the viscous VHE and inviscid DPLe cases (with a larger amplitude in the inviscid case), and are absent in Fourier's law.

VIII. COMPARISON BETWEEN LBTE AND VHE IN A RING-SHAPED GEOMETRY

In this section we compare the time-dependent solution of the LBTE with full collision matrix discussed in Fig. 4e and Supplementary Fig. S7 of Ref. [12] with the corresponding VHE solution. Specifically, we consider: (i) a device made of pure graphite (100% ^{12}C as in Ref. [12], see Tab. II for the parameters entering in the VHE in this case); (ii) a device that has $40\mu\text{m} \times 40\mu\text{m}$ section—thermalised at \bar{T} at its boundaries—and is very long in the off-plane direction; (iii) a ring-shaped heater of radius $15\mu\text{m}$, Gaussian profile with FWHM $3\mu\text{m}$, and operating for 0.4 ns at the beginning of the simulation. As in Ref. [12], we monitor the evolution of the temperature in the center of the ring-shaped perturbation. In the calculations of the transport coefficients entering in the VHE we account for microscopic phonon-boundary scattering approximatively as in Ref. [37], considering a characteristic size equal to $20\mu\text{m}$ (the radius of the largest circle that can be inscribed in the simulation domain).

We show in Fig. SF 16a) that around $\bar{T} = 80\text{K}$, the full solution of the LBTE from Ref. [12] predicts lattice cooling (normalized response $r(t) = (T(t) - \bar{T}) / (\max[T(t)] - \bar{T})$ assuming negative values) to have a magnitude and evolution timescale that are in agreement with those predicted by the VHE. We note that the magnitude of lattice cooling (minimum of the normalized response) is visibly affected by the thermal viscosity, and considering (neglecting) the viscosity using the VHE (DPLe) yields a response in better (worse) agreement with the LBTE one. In addition, we highlight how Fourier's law predicts a diffusive, always positive response that is in strong disagreement with the oscillatory behavior emerging from

the LBTE and confirmed by experiments[12].

While the VHE and LBTE predict a relaxation that is in very good agreement at the times at which lattice cooling occurs, they show differences at very short times (inset of Fig. SF 16a). As mentioned in the main text, the VHE have been derived[37] coarse-graining the LBTE for the microscopic phonon distribution function into partial differential equations for local temperature and drift-velocity fields[37]; such coarse-graining neglected gradients in space and time of the out-of-equilibrium phonon distribution. As such, the VHE are expected to be inaccurate at very short timescales (as well as at very short

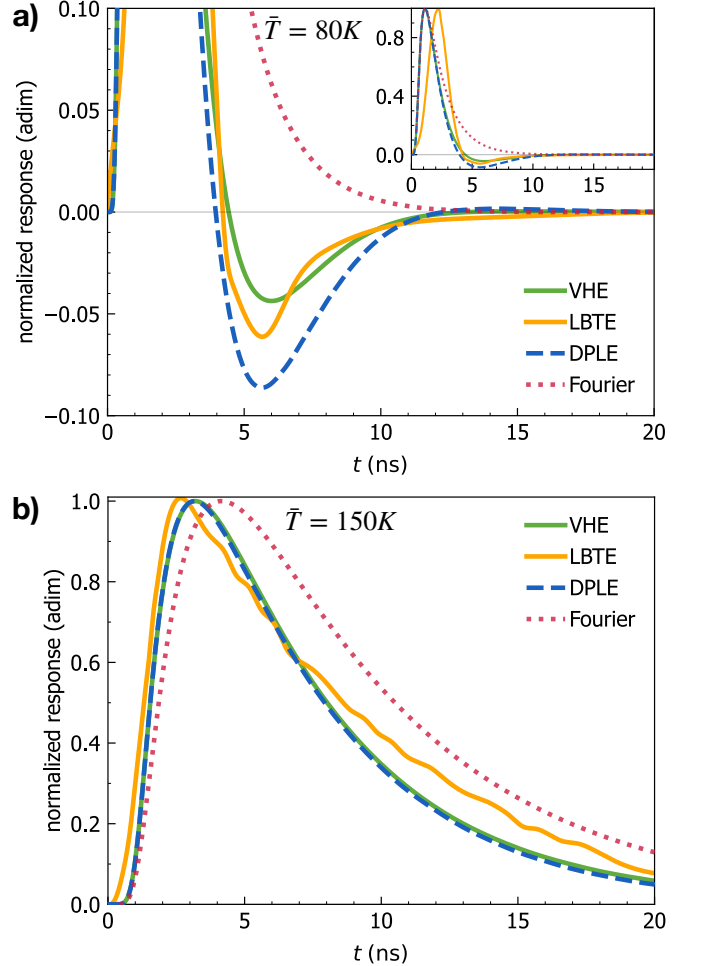


FIG. SF 16. **BTE versus VHE transient heat backflow.** We show the temporal evolution of temperature at the center of a ring-shaped perturbation analogous to that discussed in Appendix 7 of Ref. [12] (*i.e.*, isotopically purified graphite, perturbation of radius $15\mu\text{m}$). Panel a) shows that around 80K there is agreement between the oscillatory relaxation (lattice cooling) predicted by the LBTE (orange, taken from Fig. 4g of Ref. [12]) and by the VHE (green); the inviscid DPLe (dashed blue) overestimates LBTE's lattice cooling, and Fourier's law yields a diffusive (always-positive) relaxation. The inset shows the entire relaxation dynamics. Panel b) absence of hydrodynamic lattice cooling in the same device around an average temperature of 150K .

lengthscales, as discussed in Sec. V). Nevertheless, we highlight how these differences at very short times are practically irrelevant for the phenomenon of lattice cooling occurring at $5 \lesssim t \lesssim 10$ ns.

Fig. SF 16b) shows that the response predicted by the time-dependent solution of LBTE is always positive when the perturbation is applied around an average temperature of $\bar{T} = 150K$ —*i.e* lattice cooling does not occur in this case—and such behavior is in reasonable agreement with the evolution predicted by VHE. We also note that in this case the inviscid DPLE and the VHE have practically indistinguishable solutions; this shows that the thermal viscosity has negligible effects on the thermal relaxation around $\bar{T} = 150K$. Finally, at 150 K Fourier’s law predicts an always-positive, diffusive relaxation that is qualitatively similar but slightly delayed compared to the relaxations predicted by the LBTE, VHE, and DPLE; this originates from neglecting the heat carried by the drift velocity within Fourier’s law.

Overall, these results demonstrate that the VHE capture with reasonable accuracy the salient features of the time-dependent temperature relaxation emerging from the LBTE, showing that the thermal viscosity quantitatively affects transient signatures of heat hydrodynamics around $\bar{T} = 80K$.

IX. PARAMETERS ENTERING THE VISCOUS HEAT EQUATIONS

In order to simplify the notation for the parameters entering in the viscous heat equations (1,2), we defined the following parameters: $\alpha^{ji} = W_{0j}^i \sqrt{\bar{T} A^j C}$, $\beta^{ij} = \sqrt{\frac{C A^i}{\bar{T}}} W_{i0}^j$, $\gamma^{ij} = \sqrt{A^i A^j} D_U^{ij}$. In these expressions, C is the specific heat, W_{0j}^i is the velocity tensor that arises from the non-diagonal form of the diffusion operator in the basis of the eigenvectors of the normal part of the scattering matrix, \bar{T} is the reference (equilibrium) temperature on which a perturbation is applied, A^i is the specific momentum in direction i . More details on these parameters can be found in Ref. [37].

A. Graphite

All the parameters were computed from first principles, see Ref. [37] for computational details. The parameters for graphite with natural-abundance isotopic-mass disorder (98.9 % ^{12}C , 1.1 % ^{13}C) are reported in Table I of Ref. [37]. The parameters for isotopically purified samples (99.9 % ^{12}C , 0.1 % ^{13}C) are reported in Table. I, and for perfectly pure graphite (100 % ^{12}C) in Tab. II. We conclude by noting that in this work we employed the approximation of considering the parameters entering in the VHE, DPLE, and Fourier’s equation to be independent from frequency. This approximation is accurate in the MHz range considered here, as discussed by Ref. [17].

B. Monoisotopic hexagonal boron nitride

First-principles calculations have been performed with the Quantum ESPRESSO distribution [102, 103] using the the local-density approximation (LDA) for the exchange-correlation energy functional, since it has been shown to accurately describe the vibrational and thermal properties of hBN [5, 6, 104]. The pseudopotentials have been taken from the pseudo Dojo library [105] (specifically, we have used norm-conserving and scalar-relativistic pseudopotentials with accuracy “stringent” and of type ONCVSP v0.4). The crystal structure of hBN has been taken from [106] (Crystallographic Open Database [107] id 2016170). Kinetic energy cutoffs of 90 and 360 Ry have been used for the wave functions and for the charge density; the Brillouin zone (BZ) is integrated with a Monkhorst-Pack mesh of $8 \times 8 \times 3$ points, with a (1,1,1) shift. The equilibrium crystal structure has been computed performing a “vc-relax” calculation with Quantum ESPRESSO and the DFT-optimized lattice parameters are $a = 2.489089 \text{ \AA}$ and $c/a = 2.604045$. Second-order force constants have been computed on a $8 \times 8 \times 3$ mesh using density-functional perturbation theory [108] and accounting for the non-analytic term correction due to the dielectric tensor and Born effective charges. Third-order force constants have been computed using the finite-difference method implemented in SHENGBTE [97], on a $4 \times 4 \times 2$ supercell, integrating the BZ with a $2 \times 2 \times 1$ Monkhorst-Pack mesh, and considering interactions up to 3.944 \AA (which corresponds to the 6th nearest neighbor). Then, anharmonic force constants have been converted from SHENGBTE format to mat3R format using the interconversion software `d3_import_shengbte.x` provided with the D3Q package [92, 93], including interactions up to the second neighbouring cell for the re-centering of the third-order force constants (parameter NFAR=2). All the parameters entering in the VHE have been computed using a q-point mesh equal to $49 \times 49 \times 3$ and a Gaussian smearing of 6 cm^{-1} , and are reported in Table III.

TABLE I. Parameters entering the viscous heat equations for isotopically purified graphite (99.9 % ^{12}C , 0.1 % ^{13}C). We report here only the in-plane components of the tensors needed to perform the calculations: $\kappa_P^{ij} = \kappa_P \delta^{ij}$, $\kappa_C^{ij} = \kappa_C \delta^{ij}$ (see Refs. [109–112] for details on κ_C), $K_S^{ij} = K_S \delta^{ij}$, $D_{U,\text{bulk}}^{ij} = D_{U,\text{bulk}} \delta^{ij}$, $F_U^{ij} = F_U \delta^{ij}$, $A = A^i \forall i$, $W_{0i}^j = W_{i0}^j = W \delta^{ij}$, where the indexes i, j represent the in-plane directions x, y only ($i, j = 1, 2$ and $i \neq j$).

T [K]	κ_P [$\frac{\text{W}}{\text{m}\cdot\text{K}}$]	κ_C [$\frac{\text{W}}{\text{m}\cdot\text{K}}$]	K_S [$\frac{\text{W}}{\text{m}^2\cdot\text{K}}$]	$\mu_{\text{bulk}}^{\text{iii}}$ [Pa·s]	$\mu_{\text{bulk}}^{\text{ijj}}$ [Pa·s]	$\mu_{\text{bulk}}^{\text{ijji}}$ [Pa·s]	M^{iii} [$\frac{\text{Pa}\cdot\text{s}}{\text{m}}$]	M^{ijj} [$\frac{\text{Pa}\cdot\text{s}}{\text{m}}$]	M^{ijji} [$\frac{\text{Pa}\cdot\text{s}}{\text{m}}$]	$D_{U,\text{bulk}}$ [ns^{-1}]	F_U [$\frac{\text{m}}{\text{s}}$]	A [$\frac{\text{pg}}{\mu\text{m}^3}$]	C [$\frac{\text{pg}}{\mu\text{m}\cdot\text{ns}^2\cdot\text{K}}$]	W [$\frac{\mu\text{m}}{\text{ns}}$]
50	3.34175e+04	8.17849e-05	2.57075e+08	1.11244e-03	5.62103e-04	2.71810e-04	4.39176e+02	1.46638e+02	1.46269e+02	2.41659e-02	4.26877e+03	1.53433e-04	1.00900e-04	2.72761e+00
60	3.52935e+04	1.44119e-04	3.95197e+08	1.09365e-03	5.84333e-04	2.51162e-04	7.15578e+02	2.39244e+02	2.38166e+02	4.34202e-02	4.59801e+03	2.29498e-04	1.41101e-04	3.00647e+00
70	3.24978e+04	2.40448e-04	5.59073e+08	1.09700e-03	6.15163e-04	2.37329e-04	1.07264e+03	3.59308e+02	3.56661e+02	8.50411e-02	4.88642e+03	3.20256e-04	1.84524e-04	3.25249e+00
80	2.74850e+04	4.06335e-04	7.45726e+08	1.11813e-03	6.50051e-04	2.30398e-04	1.51011e+03	5.07190e+02	5.01440e+02	1.68503e-01	5.13608e+03	4.25102e-04	2.30997e-04	3.45924e+00
90	2.25348e+04	7.19062e-04	9.52361e+08	1.15613e-03	6.86615e-04	2.31108e-04	2.02532e+03	6.82641e+02	6.71286e+02	3.18608e-01	5.34894e+03	5.43532e-04	2.80534e-04	3.62371e+00
100	1.84465e+04	1.30478e-03	1.17648e+09	1.21344e-03	7.23418e-04	2.41404e-04	2.61392e+03	8.5021e+02	8.64331e+02	5.63474e-01	5.52812e+03	6.75030e-04	3.33160e-04	3.74625e+00
120	1.27814e+04	3.97919e-03	1.66857e+09	1.39850e-03	7.94571e-04	2.98592e-04	3.98943e+03	1.36695e+03	1.31087e+03	1.45053e+00	5.80204e+03	9.74775e-04	4.47442e-04	3.88006e+00
140	9.33971e+03	9.87325e-03	2.20653e+09	1.67560e-03	8.59931e-04	4.04889e-04	5.59088e+03	1.94459e+03	1.82232e+03	3.02867e+00	5.99201e+03	1.31862e-03	5.72512e-04	3.90257e+00
160	7.14426e+03	2.01725e-02	2.77632e+09	2.00642e-03	9.18230e-04	5.41712e-04	7.37504e+03	2.60822e+03	2.38191e+03	5.43535e+00	6.12653e+03	1.70002e-03	7.05946e-04	3.85826e+00
180	5.66903e+03	3.55200e-02	3.36529e+09	2.33991e-03	9.69102e-04	6.83651e-04	9.30496e+03	3.34736e+03	2.97640e+03	8.74395e+00	6.22525e+03	2.11243e-03	8.44946e-04	3.78035e+00
185	5.37644e+03	4.01659e-02	3.51416e+09	2.41895e-03	9.80665e-04	7.17548e-04	9.80654e+03	3.54269e+03	3.12927e+03	9.71528e+00	6.24592e+03	2.21967e-03	8.80257e-04	3.75825e+00
190	5.10779e+03	4.51306e-02	3.66336e+09	2.49541e-03	9.91776e-04	7.50384e-04	1.03149e+04	3.74191e+03	3.28357e+03	1.07442e+01	6.26529e+03	2.32838e-03	9.15719e-04	3.73558e+00
195	4.86054e+03	5.04083e-02	3.81277e+09	2.56902e-03	1.00244e-03	7.82019e-04	1.08297e+04	3.94485e+03	3.43919e+03	1.18304e+01	6.28349e+03	2.43848e-03	9.51302e-04	3.71251e+00
200	4.63247e+03	5.59919e-02	3.96223e+09	2.63960e-03	1.01267e-03	8.12350e-04	1.13505e+04	4.15136e+03	3.59604e+03	1.29735e+01	6.30063e+03	2.54990e-03	9.86974e-04	3.68920e+00
220	3.87676e+03	8.11890e-02	4.55837e+09	2.88966e-03	1.04937e-03	9.19634e-04	1.34874e+04	5.01005e+03	4.23388e+03	1.80998e+01	6.36031e+03	3.00734e-03	1.13005e-03	3.59566e+00
240	3.30876e+03	1.10363e-01	5.14699e+09	3.08900e-03	1.07987e-03	1.00459e-03	1.56967e+04	5.91420e+03	4.88503e+03	2.40671e+01	6.40897e+03	3.48061e-03	1.27276e-03	3.50487e+00
260	2.87089e+03	1.42551e-01	5.72314e+09	3.24372e-03	1.10492e-03	1.06990e-03	1.79634e+04	6.85568e+03	5.54605e+03	3.07981e+01	6.44952e+03	3.96638e-03	1.41411e-03	3.41888e+00
280	2.52599e+03	1.76706e-01	6.28327e+09	3.36215e-03	1.12530e-03	1.11933e-03	2.02756e+04	7.82758e+03	6.21450e+03	3.82043e+01	6.48385e+03	4.46204e-03	1.55341e-03	3.33828e+00
300	2.24925e+03	2.11805e-01	6.82487e+09	3.45227e-03	1.14175e-03	1.15650e-03	2.26238e+04	8.82402e+03	6.88860e+03	4.61938e+01	6.51324e+03	4.96554e-03	1.69010e-03	3.26300e+00
350	1.75503e+03	2.98054e-01	8.08784e+09	3.59424e-03	1.16993e-03	1.21399e-03	2.86057e+04	1.13924e+04	8.59059e+03	6.81463e+01	6.57048e+03	6.24865e-03	2.01775e-03	3.09612e+00
400	1.43431e+03	3.74983e-01	9.21271e+09	3.66698e-03	1.18574e-03	1.24278e-03	3.68484e+04	1.40297e+04	1.03064e+04	9.20012e+01	6.61114e+03	7.55350e-03	2.32135e-03	2.95575e+00

TABLE II. Parameters entering the viscous heat equations for pure graphite (100 % ^{12}C). We report here only the in-plane components of the tensors needed to perform the calculations: $\kappa_P^{ij} = \kappa_P \delta^{ij}$, $\kappa_C^{ij} = \kappa_C \delta^{ij}$, $K_S^{ij} = K_S \delta^{ij}$, $D_{U,\text{bulk}}^{ij} = D_{U,\text{bulk}} \delta^{ij}$, $F_U^{ij} = F_U \delta^{ij}$, $A = A^i \forall i$, $W_{0i}^j = W_{i0}^j = W \delta^{ij}$, where the indexes i, j represent the in-plane directions x, y only ($i, j = 1, 2$ and $i \neq j$).

T [K]	κ_P [$\frac{\text{W}}{\text{m}\cdot\text{K}}$]	κ_C [$\frac{\text{W}}{\text{m}\cdot\text{K}}$]	K_S [$\frac{\text{W}}{\text{m}^2\cdot\text{K}}$]	$\mu_{\text{bulk}}^{\text{iii}}$ [Pa·s]	$\mu_{\text{bulk}}^{\text{ijj}}$ [Pa·s]	$\mu_{\text{bulk}}^{\text{ijji}}$ [Pa·s]	M^{iii} [$\frac{\text{Pa}\cdot\text{s}}{\text{m}}$]	M^{ijj} [$\frac{\text{Pa}\cdot\text{s}}{\text{m}}$]	M^{ijji} [$\frac{\text{Pa}\cdot\text{s}}{\text{m}}$]	$D_{U,\text{bulk}}$ [ns^{-1}]	F_U [$\frac{\text{m}}{\text{s}}$]	A [$\frac{\text{pg}}{\mu\text{m}^3}$]	C [$\frac{\text{pg}}{\mu\text{m}\cdot\text{ns}^2\cdot\text{K}}$]	W [$\frac{\mu\text{m}}{\text{ns}}$]
80	5.05800e+04	4.03690e-04	7.45726e+08	1.13125e-03	6.57961e-04	2.32861e-04	1.51011e+03	5.07190e+02	5.01440e+02	1.13119e-01	5.13608e+03	4.25102e-04	2.30997e-04	3.45924e+00
150	8.76453e+03	1.42003e-02	2.48831e+09	1.85042e-03	8.99385e-04	4.72804e-04	6.46259e+03	2.26630e+03	2.09701e+03	3.94422e+00	6.06477e+03	1.50504e-03	6.38359e-04	3.88637e+00

TABLE III. Parameters entering the viscous heat equations for h^{11}BN . We report here only the in-plane components of the tensors needed to perform the calculations: $\kappa_P^{ij} = \kappa_P \delta^{ij}$, $\kappa_C^{ij} = \kappa_C \delta^{ij}$, $K_S^{ij} = K_S \delta^{ij}$, $D_{U,\text{bulk}}^{ij} = D_{U,\text{bulk}} \delta^{ij}$, $F_U^{ij} = F_U \delta^{ij}$, $A = A^i \forall i$, $W_{0i}^j = W_{i0}^j = W \delta^{ij}$, where the indexes i, j represent the in-plane directions x, y only ($i, j = 1, 2$ and $i \neq j$).

T [K]	κ_P [$\frac{\text{W}}{\text{m}\cdot\text{K}}$]	κ_C [$\frac{\text{W}}{\text{m}\cdot\text{K}}$]	K_S [$\frac{\text{W}}{\text{m}^2\cdot\text{K}}$]	$\mu_{\text{bulk}}^{\text{iii}}$ [Pa·s]	$\mu_{\text{bulk}}^{\text{ijj}}$ [Pa·s]	$\mu_{\text{bulk}}^{\text{ijji}}$ [Pa·s]	M^{iii} [$\frac{\text{Pa}\cdot\text{s}}{\text{m}}$]	M^{ijj} [$\frac{\text{Pa}\cdot\text{s}}{\text{m}}$]	M^{ijji} [$\frac{\text{Pa}\cdot\text{s}}{\text{m}}$]	$D_{U,\text{bulk}}$ [ns^{-1}]	F_U [$\frac{\text{m}}{\text{s}}$]	A [$\frac{\text{pg}}{\mu\text{m}^3}$]	C [$\frac{\text{pg}}{\mu\text{m}\cdot\text{ns}^2\cdot\text{K}}$]	W [$\frac{\mu\text{m}}{\text{ns}}$]
50	5.08496e+03	4.39299e-04	3.18233e+08	7.09609e-04	4.61623e-04	1.24381e-04	6.97634e+02	2.33387e+02	2.32121e+02	3.15987e-01	3.70983e+03	2.73574e-04	1.49113e-04	2.40299e+00
60	3.94420e+03	6.91660e-04	4.77290e+08	7.07393e-04	4.76252e-04	1.16007e-04	1.15258e+03	3.86399e+02	3.83081e+02	7.48719e-01	3.87655e+03	4.26806e-04	2.08230e-04	2.56422e+00
75	2.87382e+03	1.19669e-03	7.48233e+08	7.07296e-04	4.91045e-04	1.08615e-04	2.04154e+03	6.87240e+02	6.77105e+02	1.93310e+00	4.01963e+03	7.19449e-04	3.03986e-04	2.71119e+00
100	1.89907e+03	2.58860e-03	1.24792e+09	7.20155e-04	4.98382e-04	1.11402e-04	3.92792e+03	1.33705e+03	1.29525e+03	5.71441e+00	4.10962e+03	1.33990e-03	4.71727e-04	2.79944e+00
125	1.37164e+03	5.21646e-03	1.78806e+09	7.79727e-04	5.01978e-04	1.39347e-04	6.13109e+03	2.12395e+03	2.00311e+03	1.19136e+01	4.14080e+03	2.07076e-03	6.44647e-04	2.78843e+00
150	1.06699e+03	9.66905e-03	2.36077e+09	8.91251e-04	5.12533e-04	1.89739e-04	8.52906e+03	3.02013e+03	2.75353e+03	2.02022e+01	4.16302e+03	2.86999e-03	8.22855e-04	2.73368e+00
175	8.83008e+02	1.62740e-02	2.95342e+09	1.02915e-03	5.30428e-04	2.49625e-04	1.10622e+04	4.00902e+03	3.52496e+03	3.01303e+01	4.18665e+03	3.71435e-03	1.00492e-03	2.66425e+00
200	7.65123e+02	2.51062e-02	3.55061e+09	1.16741e-03	5.52319e-04	3.07683e-04	1.36961e+04	5.07502e+03	4.30804e+03	4.13328e+01	4.21210e+03	4.58997e-03	1.18813e-03	2.59391e+00
225	6.83803e+02	3.60584e-02	4.13896e+09	1.29214e-03	5.74869e-04	3.58660e-04	1.64072e+04	6.20280e+03	5.09861e+03	5.35343e+01	4.23792e+03	5.48778e-03	1.37008e-03	2.52756e+00
250	6.23329e+02	4.88988e-02	4.70873e+09	1.39919e-03	5.95930e-04	4.01553e-04	1.91773e+04	7.37844e+03	5.89459e+03	6.65173e+01	4.26281e+03	6.40150e-03	1.54901e-03	2.46616e+00
275	5.75413e+02	6.33176e-02	5.25353e+09	1.48916e-03	6.14491e-04	4.37170e-04	2.19921e+04	8.59015e+03	6.69477e+03	8.01021e+01	4.28596e+03	7.32669e-03	1.72367e-03	2.40940e+00
300	5.35638e+02	7.89685e-02	5.76951e+09	1.56429e-03	6.30300e-04	4.66758e-04	2.48404e+04	9.82843e+03	7.49827e+03	9.41385e+01	4.30696e+03	8.26014e-03	1.89306e-03	2.35678e+00
325	5.01567e+02	9.55019e-02	6.25468e+09	1.62704e-03	6.43502e-04	4.91475e-04	2.77130e+04	1.10858e+04	8.30433e+03	1.08503e+02	4.32573e+03	9.19946e-03	2.05633e-03	2.30792e+00
350	4.71776e+02	1.12591e-01	6.70835e+09	1.67963e-03	6.54418e-04	5.12263e-04	3.06029e+04	1.23564e+04	9.11232e+03	1.23095e+02	4.34233e+03	1.01428e-02	2.21279e-03	2.26256e+00

-
- [1] A. J. Schmidt, X. Chen, and G. Chen, Pulse accumulation, radial heat conduction, and anisotropic thermal conductivity in pump-probe transient thermoreflectance, *Rev. Sci. Instrum.* **79**, 114902 (2008).
 - [2] A. A. Balandin, Thermal properties of graphene and nanostructured carbon materials, *Nat. Mater.* **10**, 569 (2011).
 - [3] G. Fugallo, A. Cepellotti, L. Paulatto, M. Lazzeri, N. Marzari, and F. Mauri, Thermal Conductivity of Graphene and Graphite: Collective Excitations and Mean Free Paths, *Nano Lett.* **14**, 6109 (2014).
 - [4] Y. Machida, N. Matsumoto, T. Isono, and K. Behnia, Phonon hydrodynamics and ultrahigh-room-temperature thermal conductivity in thin graphite, *Science* **367**, 309 (2020).
 - [5] P. Jiang, X. Qian, R. Yang, and L. Lindsay, Anisotropic thermal transport in bulk hexagonal boron nitride, *Phys. Rev. Materials* **2**, 064005 (2018).
 - [6] C. Yuan, J. Li, L. Lindsay, D. Cherns, J. W. Pomeroy, S. Liu, J. H. Edgar, and M. Kuball, Modulating the thermal conductivity in hexagonal boron nitride via controlled boron isotope concentration, *Commun. Phys.* **2** (2019).
 - [7] X. Qian, J. Zhou, and G. Chen, Phonon-engineered extreme thermal conductivity materials, *Nat. Mater.* **20**, 1188 (2021).
 - [8] S. Moon, J. Kim, J. Park, S. Im, J. Kim, I. Hwang, and J. K. Kim, Hexagonal Boron Nitride for Next-Generation Photonics and Electronics, *Adv. Mater.* **35**, 2204161 (2023).
 - [9] G. Chen, Non-Fourier phonon heat conduction at the microscale and nanoscale, *Nat. Rev. Phys.* **3**, 555 (2021).
 - [10] X. Huang, Y. Guo, Y. Wu, S. Masubuchi, K. Watanabe, T. Taniguchi, Z. Zhang, S. Volz, T. Machida, and M. Nomura, Observation of phonon Poiseuille flow in isotopically purified graphite ribbons, *Nat. Commun.* **14**, 2044 (2023).
 - [11] S. Huberman, R. A. Duncan, K. Chen, B. Song, V. Chiloyan, Z. Ding, A. A. Maznev, G. Chen, and K. A. Nelson, Observation of second sound in graphite at temperatures above 100 K, *Science* **364**, 375 (2019).
 - [12] J. Jeong, X. Li, S. Lee, L. Shi, and Y. Wang, Transient hydrodynamic lattice cooling by picosecond laser irradiation of graphite, *Phys. Rev. Lett.* **127**, 085901 (2021).
 - [13] Z. Ding, K. Chen, B. Song, J. Shin, A. A. Maznev, K. A. Nelson, and G. Chen, Observation of second sound in graphite over 200 K, *Nat. Commun.* **13**, 285 (2022).
 - [14] Specifically, Ref. [13] observed temperature oscillations at temperatures as high as 200 K in isotopically purified graphite, while the pioneering works [11, 12] observed temperature oscillations around 80-100 K in graphite at natural isotopic abundance.
 - [15] R. E. Peierls, *Quantum theory of solids* (Oxford university press, 1955).
 - [16] L. Lindsay, A. Katre, A. Cepellotti, and N. Mingo, Perspective on *ab initio* phonon thermal transport, *J. Appl. Phys.* **126**, 050902 (2019).
 - [17] L. Chaput, Direct Solution to the Linearized Phonon Boltzmann Equation, *Phys. Rev. Lett.* **110**, 265506 (2013).
 - [18] G. Fugallo, M. Lazzeri, L. Paulatto, and F. Mauri, *Ab initio* variational approach for evaluating lattice thermal conductivity, *Phys. Rev. B* **88**, 045430 (2013).
 - [19] S. Lee, D. Broido, K. Esfarjani, and G. Chen, Hydrodynamic phonon transport in suspended graphene, *Nat. Commun.* **6**, 6290 (2015).
 - [20] A. Cepellotti and N. Marzari, Thermal Transport in Crystals as a Kinetic Theory of Relaxons, *Phys. Rev. X* **6**, 041013 (2016).
 - [21] Z. Ding, J. Zhou, B. Song, V. Chiloyan, M. Li, T.-H. Liu, and G. Chen, Phonon hydrodynamic heat conduction and knudsen minimum in graphite, *Nano Lett.* **18**, 638 (2018).
 - [22] Y. Guo, Z. Zhang, M. Bescond, S. Xiong, M. Wang, M. Nomura, and S. Volz, Size effect on phonon hydrodynamics in graphite microstructures and nanostructures, *Phys. Rev. B* **104**, 075450 (2021).
 - [23] X. Li, H. Lee, E. Ou, S. Lee, and L. Shi, Reexamination of hydrodynamic phonon transport in thin graphite, *J. Appl. Phys.* **131**, 075104 (2022).
 - [24] X. Huang, Y. Guo, S. Volz, and M. Nomura, Mapping phonon hydrodynamic strength in micrometer-scale graphite structures, *Appl. Phys. Express* **15**, 105001 (2022).
 - [25] A. Cepellotti, G. Fugallo, L. Paulatto, M. Lazzeri, F. Mauri, and N. Marzari, Phonon hydrodynamics in two-dimensional materials, *Nat. Commun.* **6**, 6400 (2015).
 - [26] A. K. Majee and Z. Aksamija, Dynamical thermal conductivity of suspended graphene ribbons in the hydrodynamic regime, *Phys. Rev. B* **98**, 024303 (2018).
 - [27] M. Raya-Moreno, J. Carrete, and X. Cartoixa, Hydrodynamic signatures in thermal transport in devices based on two-dimensional materials: An *ab initio* study, *Phys. Rev. B* **106**, 014308 (2022).
 - [28] Y. Guo, Z. Zhang, M. Nomura, S. Volz, and M. Wang, Phonon vortex dynamics in graphene ribbon by solving Boltzmann transport equation with *ab initio* scattering rates, *Int. J. Heat Mass Transf.* **169**, 120981 (2021).
 - [29] C. Zhang, S. Huberman, and L. Wu, On the emergence of heat waves in the transient thermal grating geometry, *J. Appl. Phys.* **132**, 085103 (2022).
 - [30] Z. Han and X. Ruan, Thermal conductivity of monolayer graphene: Convergent and lower than diamond, *Phys. Rev. B* **108**, L121412 (2023).
 - [31] A. Cepellotti and N. Marzari, Boltzmann Transport in Nanostructures as a Friction Effect, *Nano Lett.* **17**, 4675 (2017).
 - [32] Y. Machida, A. Subedi, K. Akiba, A. Miyake, M. Tokunaga, Y. Akahama, K. Izawa, and K. Behnia, Observation of Poiseuille flow of phonons in black phosphorus, *Sci. Adv.* **4**, eaat3374 (2018).
 - [33] L. Sendra, A. Beardo, J. Bafaluy, P. Torres, F. X. Alvarez, and J. Camacho, Hydrodynamic heat transport in dielectric crystals in the collective limit and the drifting/driftless velocity conundrum, *Phys. Rev. B* **106**, 155301 (2022).
 - [34] X. Li and S. Lee, Role of hydrodynamic viscosity on phonon transport in suspended graphene, *Phys. Rev. B* **97**, 094309 (2018).

- [35] Y. Guo, D. Jou, and M. Wang, Nonequilibrium thermodynamics of phonon hydrodynamic model for nanoscale heat transport, *Phys. Rev. B* **98**, 104304 (2018).
- [36] M.-Y. Shang, C. Zhang, Z. Guo, and J.-T. Lü, Heat vortex in hydrodynamic phonon transport of two-dimensional materials, *Sci. Rep.* **10**, 8272 (2020).
- [37] M. Simoncelli, N. Marzari, and A. Cepellotti, Generalization of Fourier's law into viscous heat equations, *Phys. Rev. X* **10**, 011019 (2020).
- [38] L. Sendra, A. Beardo, P. Torres, J. Bafaluy, F. X. Alvarez, and J. Camacho, Derivation of a hydrodynamic heat equation from the phonon Boltzmann equation for general semiconductors, *Phys. Rev. B* **103**, L140301 (2021).
- [39] D. D. Joseph and L. Preziosi, Heat waves, *Rev. Mod. Phys.* **61**, 41 (1989).
- [40] D. Y. Tzou, A Unified Field Approach for Heat Conduction From Macro- to Micro-Scales, *J Heat Transf* **117**, 8 (1995).
- [41] *i.e.*, when $\mu_{\max} \rightarrow 0$ and $[\gamma_{\max}]^{-1} \rightarrow 0$, where μ_{\max} and γ_{\max} are the maximum component of the viscosity and Umklapp dissipation tensors.
- [42] C. Cattaneo, A form of heat-conduction equations which eliminates the paradox of instantaneous propagation, *Comptes Rendus* **247**, 431 (1958).
- [43] We investigate monoisotopic h^{11}BN because Refs. [6, 113] suggest that heat hydrodynamics in h^{11}BN is stronger than in hexagonal boron nitride with natural isotopic-mass disorder (19.9% ^{10}B and 80.1% ^{11}B).
- [44] A. Aharon-Steinberg, T. Völkl, A. Kaplan, A. K. Pariari, I. Roy, T. Holder, Y. Wolf, A. Y. Meltzer, Y. Myasoedov, M. E. Huber, B. Yan, G. Falkovich, L. S. Levitov, M. Hückler, and E. Zeldov, Direct observation of vortices in an electron fluid, *Nature* **607**, 74 (2022).
- [45] F. Menges, H. Riel, A. Stemmer, and B. Gotsmann, Nanoscale thermometry by scanning thermal microscopy, *Rev. Sci. Instrum.* **87**, 074902 (2016).
- [46] Z. Cheng, X. Ji, and D. G. Cahill, Battery absorbs heat during charging uncovered by ultra-sensitive thermometry, *J. Power Sources* **518**, 230762 (2022).
- [47] D. G. Cahill, P. V. Braun, G. Chen, D. R. Clarke, S. Fan, K. E. Goodson, P. Keblinski, W. P. King, G. D. Mahan, A. Majumdar, H. J. Maris, S. R. Phillpot, E. Pop, and L. Shi, Nanoscale thermal transport. II. 2003–2012, *Appl. Phys. Rev.* **1**, 011305 (2014).
- [48] O. Braun, R. Furrer, P. Butti, K. Thodkar, I. Shorubalko, I. Zardo, M. Calame, and M. L. Perrin, Spatially mapping thermal transport in graphene by an opto-thermal method, *NPJ 2D Mater. Appl.* **6**, 1 (2022).
- [49] A. Ziabari, P. Torres, B. Vermeersch, Y. Xuan, X. Cartoixà, A. Torelló, J.-H. Bahk, Y. R. Koh, M. Parsa, P. D. Ye, F. X. Alvarez, and A. Shakouri, Full-field thermal imaging of quasiballistic crosstalk reduction in nanoscale devices, *Nat. Commun.* **9**, 255 (2018).
- [50] We recall that the curl of a gradient is zero, thus Fourier's heat flux $\mathbf{Q}^\delta = -\kappa \nabla T$ is irrotational.
- [51] J. M. Ziman, *Electrons and phonons: the theory of transport phenomena in solids* (Oxford university press, 1960).
- [52] N. K. Ravichandran, H. Zhang, and A. J. Minnich, Spectrally Resolved Specular Reflections of Thermal Phonons from Atomically Rough Surfaces, *Phys. Rev. X* **8**, 041004 (2018).
- [53] From a mathematical viewpoint, slipping boundaries correspond to having drift-velocity component orthogonal to the boundary equal to zero while allowing the component parallel to the boundary to be non-zero.
- [54] A. Cepellotti and N. Marzari, Transport waves as crystal excitations, *Phys. Rev. Materials* **1**, 045406 (2017).
- [55] C. Zhang and Z. Guo, A transient heat conduction phenomenon to distinguish the hydrodynamic and (quasi) ballistic phonon transport, *Int. J. Heat Mass Transf.* **181**, 121847 (2021).
- [56] M. Xu and L. Wang, Thermal oscillation and resonance in dual-phase-lagging heat conduction, *Int. J. Heat Mass Transf.* **45**, 1055 (2002).
- [57] J. Ordóñez-Miranda and J. J. Alvarado-Gil, Exact solution of the dual-phase-lag heat conduction model for a one-dimensional system excited with a periodic heat source, *Mech. Res. Commun.* **37**, 276 (2010).
- [58] Z. Kang, P. Zhu, D. Gui, and L. Wang, A method for predicting thermal waves in dual-phase-lag heat conduction, *Int. J. Heat Mass Transf.* **115**, 250 (2017).
- [59] M. Gandolfi, G. Benetti, C. Glorieux, C. Giannetti, and F. Banfi, Accessing temperature waves: A dispersion relation perspective, *Int. J. Heat Mass Transf.* **143**, 118553 (2019).
- [60] M. Xu, Thermal oscillations, second sound and thermal resonance in phonon hydrodynamics, *Proc. Math. Phys. Eng.* **477**, 20200913 (2021).
- [61] G. Mazza, M. Gandolfi, M. Capone, F. Banfi, and C. Giannetti, Thermal dynamics and electronic temperature waves in layered correlated materials, *Nat. Commun.* **12**, 6904 (2021).
- [62] In this time-dependent simulation we choose an equilibrium temperature of 80 K to match the temperature at which transient hydrodynamic heat propagation has been observed in recent experiments [11, 12].
- [63] To ensure that the perturbation created causes variations within 10% of the equilibrium temperature, we used the following parameters: $\mathcal{H} = 0.013 \frac{\text{W}}{\mu\text{m}^3}$, $t_{\text{heat}} = 0.4 \text{ ns}$, $x_c = 5 \mu\text{m}$, $\sigma_x = 2 \mu\text{m}$, $\sigma_y = 2.8 \mu\text{m}$.
- [64] D. Skinner, *Mathematical Methods*, University of Cambridge.
- [65] We report the length of the longest side, the shortest side is 0.8 times shorter.
- [66] Refs. [11, 13] quantified the hydrodynamic strength as the dip depth of the TTG signal, see e.g. Fig. 1a in Ref. [13].
- [67] A. Barletta and E. Zanchini, Hyperbolic heat conduction and thermal resonances in a cylindrical solid carrying a steady-periodic electric field, *Int. J. Heat Mass Transf.* **39**, 1307 (1996).
- [68] All the simulations shown in Fig. 3 were performed accounting for grain-boundary scattering as in Ref. [37], and considering a grain size of 20 μm . This value was estimated considering the largest grains in Fig. S3 of Ref. [11], Fig. S1 of Ref. [12], Fig. S11 of Ref. [13], and Fig. 1e of Ref. [6], which are all in broad agreement with 20 μm .
- [69] Experiments [13] for isotopically purified graphite are available only at temperatures higher than 100 K, preventing us to compare VHE and DPLE in the low-temperature limit, where Fig. 4a,b show that viscous effects are largest.
- [70] M. Raya-Moreno, X. Cartoixà, and J. Carrete, BTE-Barna: An extension of almaBTE for thermal simula-

- tion of devices based on 2D materials, *Computer Physics Communications* **281**, 108504 (2022).
- [71] S. L. Sobolev and W. Dai, Heat Transport on Ultrashort Time and Space Scales in Nanosized Systems: Diffusive or Wave-like?, *Materials* **15**, 4287 (2022).
- [72] S. L. Sobolev, Hyperbolic heat conduction, effective temperature, and third law for nonequilibrium systems with heat flux, *Physical Review E* **97**, 022122 (2018).
- [73] U. Vool, A. Hamo, G. Varnavides, Y. Wang, T. X. Zhou, N. Kumar, Y. Dovzhenko, Z. Qiu, C. A. C. Garcia, A. T. Pierce, J. Gooth, P. Anikeeva, C. Felser, P. Narang, and A. Yacoby, Imaging phonon-mediated hydrodynamic flow in WTe₂, *Nat. Phys* **17**, 1216 (2021).
- [74] H.-Y. Yang, X. Yao, V. Plisson, S. Mozaffari, J. P. Scheifers, A. F. Savvidou, E. S. Choi, G. T. McCandless, M. F. Padlewski, C. Putzke, P. J. W. Moll, J. Y. Chan, L. Balicas, K. S. Burch, and F. Tafti, Evidence of a coupled electron-phonon liquid in NbGe₂, *Nat. Commun.* **12**, 5292 (2021).
- [75] A. Jaoui, A. Gourgout, G. Seyfarth, A. Subedi, T. Lorenz, B. Fauqué, and K. Behnia, Formation of an Electron-Phonon Bifluid in Bulk Antimony, *Phys. Rev. X* **12**, 031023 (2022).
- [76] X. Huang and A. Lucas, Electron-phonon hydrodynamics, *Phys. Rev. B* **103**, 155128 (2021).
- [77] N. H. Protik, C. Li, M. Pruneda, D. Broido, and P. Ordejón, The elphbolt ab initio solver for the coupled electron-phonon Boltzmann transport equations, *NPJ Comput. Mater* **8**, 28 (2022).
- [78] A. Levchenko and J. Schmalian, Transport properties of strongly coupled electron-phonon liquids, *Ann. Phys.* **419**, 168218 (2020).
- [79] J. Coulter, R. Sundaraman, and P. Narang, Microscopic origins of hydrodynamic transport in the type-II Weyl semimetal WP₂, *Phys. Rev. B* **98**, 115130 (2018).
- [80] X.-Y. Wei, O. A. Santos, C. H. S. Lusero, G. E. W. Bauer, J. Ben Youssef, and B. J. van Wees, Giant magnon spin conductivity in ultrathin yttrium iron garnet films, *Nat. Mater.* , 1352 (2022).
- [81] H. D. Rosales, F. A. G. Albarracín, P. Pujol, and L. D. C. Jaubert, Skyrmion fluid and bimeron glass protected by a chiral spin liquid on a kagome lattice, *Phys. Rev. Lett.* **130**, 106703 (2023).
- [82] J. Bear, *Dynamics of fluids in porous media* (Courier Corporation, 2013).
- [83] We note that the VHE have a mathematical form analogous to the damped and diffusion-extended Navier-Stokes equations, used to describe rarefied fluids flowing in porous media in isothermal and laminar conditions, with VHE's temperature mapping to fluid's pressure and VHE's drift velocity mapping to fluid velocity. To see this, we highlight how the linear damping term $-\gamma^{ij}u^j(\mathbf{r}, t)$ appearing in the second VHE (2) is analogous to the dissipative term appearing in the linearized "damped" Navier-Stokes equations [114–118] used e.g. to describe a fluid flowing through a porous media. Then, the diffusive term appearing in the first VHE (1) $-\kappa^{ij}\frac{\partial^2 T(\mathbf{r}, t)}{\partial r^i \partial r^j}$ is analogous to the self-diffusion term appearing for pressure in the extended Navier-Stokes equations [119–121] used to describe the flow of an isothermal, compressible, and rarefied gas [122, 123].
- [84] The simulations in Fig. 1 were performed using LLW=0.1 μm and $F = 10^3$, i.e. the same values used for the dotted-green simulation in Fig. SF 2.
- [85] Strictly speaking, in proximity of a perfectly thermalized boundary (temperature fixed at a certain value and $\mathbf{u} = \mathbf{0}$), the temperature gradient emerging from the VHE is weakly space dependent, due to the coupling between the temperature gradient and the drift velocity in Eq. (2). In practice, in a rectangular geometry of graphite with gradient applied around 70 K, the temperature gradient and drift velocity reach a practically space-independent value within about 1 μm from the boundaries. Analytical details on the mechanisms determining this lengthscale can be found in Appendix G of Ref. [37], and numerical simulations in Fig. 4 of the same reference.
- [86] For a well-behaved vector field, the circulation computed on a closed streamline $\vec{\mathcal{S}}$ is nonzero: $\mathcal{C} = \oint_{\vec{\mathcal{S}}} \mathbf{Q}^D \cdot d\vec{\mathcal{S}} \neq 0$; therefore, one sees from Stokes' theorem that this implies non-zero vorticity: $\mathcal{C} = \int_{\mathcal{A}} (\nabla \times \mathbf{Q}^D) \cdot \mathbf{m} d\mathcal{A} \neq 0$, where \mathbf{m} is the versor outward-normal to the surface \mathcal{A} enclosed by $\vec{\mathcal{S}}$.
- [87] Specifically, in the region where temperature inversion is most pronounced in Fig. 1, one has $\beta \frac{\partial T(\mathbf{r}, t)}{\partial r^y} \sim \mu^{yyyy} \frac{\partial^2 u^y(\mathbf{r}, t)}{\partial r_y^2}$, a condition that permits temperature gradient and drift velocity to be aligned, thus temperature-gradient heat flux $\mathbf{Q}^{\delta} = -\kappa \nabla T$ and drifting heat flux $\mathbf{Q}^D = \alpha \mathbf{u}$ to have opposite directions.
- [88] J.-P. M. Péraud and N. G. Hadjiconstantinou, Efficient simulation of multidimensional phonon transport using energy-based variance-reduced Monte Carlo formulations, *Physical Review B* **84**, 205331 (2011).
- [89] P. B. Allen and V. Perebeinos, Temperature in a Peierls-Boltzmann treatment of nonlocal phonon heat transport, *Physical Review B* **98**, 085427 (2018).
- [90] H. Spohn, The Phonon Boltzmann Equation, Properties and Link to Weakly Anharmonic Lattice Dynamics, *Journal of Statistical Physics* **124**, 1041 (2006).
- [91] The VHE solution in Fig. 1 was computed in less than two minutes on a laptop, while the corresponding LBTE solution in Fig. SF 8 took about 72 hours on one node (128 cores) of the Kelvin2 supercomputer from the Northern Ireland High Performance Computing center.
- [92] L. Paulatto, F. Mauri, and M. Lazzeri, Anharmonic properties from a generalized third-order ab initio approach: Theory and applications to graphite and graphene, *Phys. Rev. B* **87**, 214303 (2013).
- [93] L. Paulatto, I. Errea, M. Calandra, and F. Mauri, First-principles calculations of phonon frequencies, lifetimes, and spectral functions from weak to strong anharmonicity: The example of palladium hydrides, *Phys. Rev. B* **91**, 054304 (2015).
- [94] A. Togo, First-principles Phonon Calculations with Phonopy and Phono3py, *Journal of the Physical Society of Japan* **92**, 012001 (2023).
- [95] <https://phonopy.github.io/phonopy/qe.html>.
- [96] Thermal2 module, <https://github.com/anharmonic/d3q/tree/main/thermal2>.
- [97] W. Li, J. Carrete, N. A. Katcho, and N. Mingo, ShengBTE: A solver of the Boltzmann transport equation for phonons, *Comput. Phys. Commun.* **185**, 1747 (2014).
- [98] M. Raya-Moreno, *Heat transport in binary semiconductor polytypes and devices based on 2D materials: an ab initio study*, Ph.D. thesis.

- [99] S.-i. Tamura, Isotope scattering of dispersive phonons in Ge, *Physical Review B* **27**, 858 (1983).
- [100] L. W. Tu, *An Introduction to Manifolds* (Springer Science + Business Media, LLC, 2008) pp. 127–130.
- [101] F. Phillips, SmootherStep: An improved sigmoidal interpolation function, <https://resources.wolframcloud.com/FunctionRepository/resources/SmootherStep/> (2019).
- [102] P. Giannozzi, S. Baroni, N. Bonini, M. Calandra, R. Car, C. Cavazzoni, D. Ceresoli, G. L. Chiarotti, M. Cococcioni, I. Dabo, *et al.*, QUANTUM ESPRESSO: a modular and open-source software project for quantum simulations of materials, *J. Phys. Condens. Matter* **21**, 395502 (2009).
- [103] P. Giannozzi, O. Andreussi, T. Brumme, O. Bunau, M. B. Nardelli, M. Calandra, R. Car, C. Cavazzoni, D. Ceresoli, M. Cococcioni, N. Colonna, I. Carnimeo, A. D. Corso, S. de Gironcoli, P. Delugas, R. A. D. Jr, A. Ferretti, A. Floris, G. Fratesi, G. Fugallo, R. Gebauer, U. Gerstmann, F. Giustino, T. Gorni, J. Jia, M. Kawamura, H.-Y. Ko, A. Kokalj, E. Küçükbenli, M. Lazzeri, M. Marsili, N. Marzari, F. Mauri, N. L. Nguyen, H.-V. Nguyen, A. O. de-la Roza, L. Paulatto, S. Poncè, D. Rocca, R. Sabatini, B. Santra, M. Schlipf, A. P. Seitsonen, A. Smogunov, I. Timrov, T. Thonhauser, P. Umari, N. Vast, X. Wu, and S. Baroni, Advanced capabilities for materials modelling with Quantum ESPRESSO, *J. Phys. Condens. Matter* **29**, 465901 (2017).
- [104] R. Cuscó, L. Artús, J. H. Edgar, S. Liu, G. Cassabois, and B. Gil, Isotopic effects on phonon anharmonicity in layered van der waals crystals: Isotopically pure hexagonal boron nitride, *Phys. Rev. B* **97**, 155435 (2018).
- [105] M. Van Setten, M. Giantomassi, E. Bousquet, M. J. Verstraete, D. R. Hamann, X. Gonze, and G.-M. Rignanese, The pseudodojo: Training and grading a 85 element optimized norm-conserving pseudopotential table, *Comput. Phys. Commun.* **226**, 39 (2018).
- [106] O. O. Kurakevych and V. L. Solozhenko, Rhombohedral boron subnitride, B_3N_2 , by X-ray powder diffraction, *Acta Crystallogr., Sect. C* **63**, i80 (2007).
- [107] S. Gražulis, D. Chateigner, R. T. Downs, A. F. T. Yokochi, M. Quirós, L. Lutterotti, E. Manakova, J. Butkus, P. Moeck, and A. Le Bail, Crystallography Open Database – an open-access collection of crystal structures, *J. Appl. Crystallogr.* **42**, 726 (2009).
- [108] S. Baroni, S. de Gironcoli, A. Dal Corso, and P. Giannozzi, Phonons and related crystal properties from density-functional perturbation theory, *Rev. Mod. Phys.* **73**, 515 (2001).
- [109] Simoncelli, M. and Marzari, N. and Mauri, F., Unified theory of thermal transport in crystals and glasses, *Nat. Phys.* **15**, 809 (2019).
- [110] M. Simoncelli, N. Marzari, and F. Mauri, Wigner formulation of thermal transport in solids, *Phys. Rev. X* **12**, 041011 (2022).
- [111] G. Caldarelli, M. Simoncelli, N. Marzari, F. Mauri, and L. Benfatto, Many-body Green’s function approach to lattice thermal transport, *Phys. Rev. B* **106**, 024312 (2022).
- [112] E. Di Lucente, M. Simoncelli, and N. Marzari, Crossover from boltzmann to wigner thermal transport in thermoelectric skutterudites, *Phys. Rev. Res.* **5**, 033125 (2023).
- [113] M. Simoncelli, *Thermal transport beyond Fourier, and beyond Boltzmann*, Ph.D. thesis, École polytechnique fédérale de Lausanne (2021).
- [114] K. Balasubramanian, F. Hayot, and W. F. Saam, Darcy’s law from lattice-gas hydrodynamics, *Phys. Rev. A* **36**, 2248 (1987).
- [115] O. Dardis and J. McCloskey, Lattice Boltzmann scheme with real numbered solid density for the simulation of flow in porous media, *Phys. Rev. E* **57**, 4834 (1998).
- [116] D. Bresch and B. Desjardins, Existence of Global Weak Solutions for a 2D Viscous Shallow Water Equations and Convergence to the Quasi-Geostrophic Model, *Commun. Math. Phys.* **238**, 211 (2003).
- [117] X. Cai and Q. Jiu, Weak and strong solutions for the incompressible Navier–Stokes equations with damping, *J. Math. Anal.* **343**, 799 (2008).
- [118] Z. Zhang, X. Wu, and M. Lu, On the uniqueness of strong solution to the incompressible Navier–Stokes equations with damping, *J. Math. Anal.* **377**, 414 (2011).
- [119] H. Brenner, Navier–Stokes revisited, *Physica A* **349**, 60 (2005).
- [120] R. Sambasivam, S. Chakraborty, and F. Durst, Numerical predictions of backward-facing step flows in microchannels using extended Navier–Stokes equations, *Microfluid. Nanofluid.* **16**, 757 (2014).
- [121] J. Schwarz, K. Axelsson, D. Anheuer, M. Richter, J. Adam, M. Heinrich, and R. Schwarze, An OpenFOAM solver for the extended Navier–Stokes equations, *SoftwareX* **22**, 101378 (2023).
- [122] J. Maurer, P. Tabeling, P. Joseph, and H. Willaime, Second-order slip laws in microchannels for helium and nitrogen, *Phys. Fluids* **15**, 2613 (2003).
- [123] N. Dongari, A. Sharma IITK, and F. Durst, Pressure-driven diffusive gas flows in micro-channels: From the Knudsen to the continuum regimes, *Microfluid. Nanofluid.* **6**, 679 (2009).